KeA1

CHINESE ROOTS
GLOBAL IMPACT

Contents lists available at ScienceDirect

Petroleum Science

journal homepage: www.keaipublishing.com/en/journals/petroleum-science



Original Paper

Dynamic characteristics of anisotropic shale and rock-breaking efficiency of the axe-shaped tooth under different impact load-bedding angles



Yan Xi ^a, Yu Yao ^a, Hong-Ao Zhao ^b, Qian Li ^{c, d}, Jun Li ^e, Ying-Chun Chen ^{a, *}

- ^a Beijing University of Technology, Beijing, 100124, China
- ^b Ocean University of China, Qingdao, 266100, Shandong, China
- ^c Sinopec Shanghai Offshore Oil and Gas Branch, Shanghai, 200120, China
- d Sinopec Offshore Oil Engineering Co., LTD, Shanghai, 200120, China
- ^e China University of Petroleum-Beijing at Karamay, Karamay, 834000, Xinjiang, China

ARTICLE INFO

Article history: Received 9 October 2024 Received in revised form 24 March 2025 Accepted 24 March 2025 Available online 25 March 2025

Edited by Jia-Jia Fei

Keywords:
Anisotropic shale
Dynamic impact
Axe-shaped teeth
Rock-breaking mechanism

ABSTRACT

Percussion drilling technology can be used to increase the rate of penetration in deep shale reservoirs, but the interaction mechanism among impact loads, drilling teeth and rock has not been sufficiently investigated. For this reason, shales with different bedding angles are used to carry out impact compression and tensile experiments as well as the rock-breaking experiments by single axe-shaped tooth, the variation of dynamic strengths, rock failure characteristics, fractal dimensions, and tensile/ compression ratios under different load-bedding angles (α) are investigated. Then, the three-dimensional scanning device is used to measure the penetration depth and rock-breaking volume under different load-bedding angles. The results show that with the increase of load-bedding angle $(0^{\circ}-90^{\circ})$, the compressive strength decreases and then increases, with the lowest strength at $\alpha=45^{\circ}$ and the highest strength at $\alpha = 0^{\circ}$; the tensile strength decreases and then increases, with the lowest strength near $\alpha=30^{\circ}$ and the highest strength at $\alpha=90^{\circ}$. With the growing impact rate, the effect of load-bedding angle on dynamic compressive strength decreases, and the effect on dynamic tensile strength becomes more significant. When the impact velocity is high $(\ge 8.0 \text{ m/s})$, the tensile-compressive ratio first decreases and then increases, and both reach a minimum at a load-bedding angle of 30° and a maximum at 60°. With the increasing of the load-bedding angle, the depth of tooth penetration increases and then decreases, and the highest depth of tooth penetration and the highest energy absorption efficiency are achieved at $\alpha = 45^{\circ}$; the width of the impact pit increases and then decreases, and the maximum width value is achieved at $\alpha = 30^{\circ}$, with the smallest value of the specific work value of the rock-breaking. The results have significant reference value for improving the rock-breaking efficiency of percussion drilling in deep anisotropic formations.

© 2025 The Authors. Publishing services by Elsevier B.V. on behalf of KeAi Communications Co. Ltd. This is an open access article under the CC BY license (http://creativecommons.org/licenses/by/4.0/).

1. Introduction

With the deepening of shale oil and gas exploration and development, organic-rich deep shale oil and gas reservoirs (vertical depth >3500 m) have received more and more attention and gradually become the target of oil and gas exploration (Gale et al., 2014; Shi et al., 2018). However, due to the high matrix strength, poor drillability and abrasive nature of deep shale reservoirs, the

rock-breaking efficiency of conventional drilling techniques is low; in addition, low penetration rate and wear of drill teeth have severely limited the development of deep shale oil and gas (Liu et al., 2021a; Peng et al., 2022). Given this, impact rock-breaking technology has been introduced into the drilling engineering of deep shale oil and gas reservoirs, and it has achieved remarkable results in improving penetration rate and rock-breaking efficiency (Amar et al., 2019). However, the rock-breaking mechanism of PDC drilling teeth under impact load is not sufficiently studied (Zhu et al., 2022; Ke et al., 2023). In addition, the shale matrix is anisotropic, and its dynamics change with the angle of the formation, and the direction of the wellbore structure affects the angle

^{*} Corresponding author. E-mail address: ychen08089@163.com (Y.-C. Chen).

between the impact load and the shale formation, which leads to a highly complex interaction between the direction of the impact load, the direction of the shale formation, and the PDC drilling teeth. Therefore, to reveal the rock-breaking mechanism of drilling teeth under impact load in deep shale reservoirs, the angle between impact load direction and shale formation direction should be considered, to lay the foundation for the establishment of the compatibility between the three, and then provide a reference to improve the mechanical rotation speed and prolong the service life of impact drilling tools.

Sedimentation during the formation of shale reservoirs causes the establishment of significant transverse isotropy in rocks, which makes the shale anisotropic in terms of mechanical properties (Alsuwaidi et al., 2021; Cui and Si, 2021; Qin et al., 2022). In this regard, many scholars have conducted experimental studies on the anisotropy of shale mechanical properties (Bobko et al., 2008; Guo and Zhang, 2014; He et al., 2022). Through triaxial compression tests on shales with different bedding directions, Fjær and Nes (2014) analyzed the anisotropic features of shale compressive strength under static conditions, and their test results showed that the failure plane of shale was affected by both the loading direction and the stratification plane. Liu et al. (2021b) drilled shale cores in Changning Block, Sichuan Basin of China, and conducted shale mechanical tests at different bedding angles. Their results demonstrated that the tensile strength of shale decreased with the increase of bedding angle, while its compressive strength presented a U-shaped variation with the change of bedding angle. Previous studies have focused on conducting static tests of shale. However, the percussion drills generate stress waves by relying mainly on the hammer reciprocating movement, thereby assisting rock breakage, which already belongs to the category of rock dynamics. Hence, analyzing the variation law of rock dynamic strength is necessary while considering shale anisotropy (Cao et al., 2022; Huang et al., 2022). Using the Split Hopkinson Pressure Bar (SHPB) test device, Yang G.L. et al. (2020) conducted dynamic compression tests on shales with different bedding angles, finding that the dynamic compressive strength of shale presented a "V" curve variation with the increase of bedding angle. Through the Brazil split test under impact load, Feng et al. (2023) analyzed the influence of shale anisotropy on the dynamic tensile strength, revealing that the tensile strength of vertically bedded shale was usually higher than that of parallel bedded shale, the deformation and fracture response of shale under dynamic load were more sensitive to strain rate. From the above literature, it is obvious that although existing studies have been conducted to experiment on the dynamic properties of shale under impact loading, most of the studies have focused on the effect of the angle of the laminations on the strength. However, in actual drilling engineering, there is an angle between the direction of impact load influenced by the wellbore trajectory and the shale bedding, and the related studies are not yet sufficient.

During the rock breakage by percussion drills, the interaction between drill cutter tooth and rock should be considered in addition to the characteristics of shale dynamics. Given the different rock-breaking mechanisms of different types of drill cutter teeth, experiments, and numerical simulation studies have been carried out previously on the teeth of different types of PDC bits (Ju et al., 2014; Akbari and Miska, 2016; Chen et al., 2021; Li et al., 2022). Negm et al. (2016) reported that axe-shaped teeth combined the squeezing and shearing actions of conventional drill cutter teeth under the drill string load, enabling easier rock formation penetration. Shao et al. (2021) conducted a wear resistance test on the PDC bit tooth, pinpointing that with higher wear resistance than the planar tooth, the axe-shaped tooth had a longer life in the rock-breaking process and was suitable for long well section drilling

applications. Through finite element numerical simulation, He et al. (2021) analyzed the rock stress distribution and strain characteristics during the conventional well drilling process with specialshaped teeth (axe-shaped and triangular), and their results demonstrated easier rock penetration and better rock-breaking efficiency by the axe-shaped tooth. By establishing numerical models of shale fragmentation with axe-shaped, triangular, and planar teeth. Dong et al. (2022) analyzed the rock-breaking effect of different types of drill cutter teeth, stating that under an equivalent static load of the drill string, the axe-shaped tooth had greater penetration depth. As is evident from the above literature, previous studies focused on the rock-breaking effect of drill cutter teeth under static load of drilling string, which failed to analyze the dynamic load generated by percussion drill. Additionally, the influence of shale anisotropy on the rock-breaking effect by drill cutter teeth was not considered in the interaction between cutter teeth and rock

Based on the above analyses, there are few studies concerning the interaction mechanism among impact load, drill bit teeth, and bedded shale during the application of percussion drilling technology in deep shale formations. This is primarily attributable to the following two challenges: (1) Under impact load, the influence of shale anisotropy on the rock dynamic strength needs to be systematically explored, including dynamic compression and tensile tests on rocks. Besides, considering both the bedding angle of shale and the angle between impact load and stratification plane is required, which will consume a long period and high cost. (2) Ouantitative evaluation of the anisotropic rock breaking effect of drill cutter teeth under impact load remains insufficient. When conducting relevant tests, it is necessary to consider the geometry of drill cutter teeth used in the engineering. Meanwhile, it is also required to fit the impact load parameters to the engineering site as much as possible. Additionally, quantitative analysis of the fragmentation morphology of rock after impact fragmentation is required, along with calculation of the rock fragmentation specific energy of drill cutter teeth at different impact velocities and bedding angles. Hence, it is imperative to experimentally investigate the dynamics characteristics of anisotropic shale under impact load and the rock breakage by drill cutter teeth.

In this research, the SHPB test is used to conduct the conventional impact test and PDC tooth impact test on bedded shale, and the load-bedding angles are used as the analyzing variable to study the mechanical properties and crushing characteristics of bedded shale under the conventional impact conditions, based on which, the depth of intrusion of bedded shale and the volume of rock breakage under the impact of a single tooth are analyzed by using the impact of the PDC tooth to calculate the specific work of rock breakage required to intrude bedded shale under different impact loads. Then, we calculate the specific work of rock breaking required to intrude into bedded shale under different load-bedding angles, which reveals the rock-breaking mechanism of PDC drill teeth under impact load. The results of this research provide a valuable reference for improving the rock-breaking efficiency of percussion drills in deep anisotropic formations, increasing the rate of penetration and prolonging the lives of percussion drills and bits.

2. Materials and methods

During rock breakage with percussion drill in deep shale stratum, the following two aspects should be considered (Fig. 1).

(1) Shale reservoir's significant stratification (anisotropy) characteristics affect the dynamic strength. During the percussion drill, the impact load generated by the hammer is transferred to the cutter tooth, which will cause rock

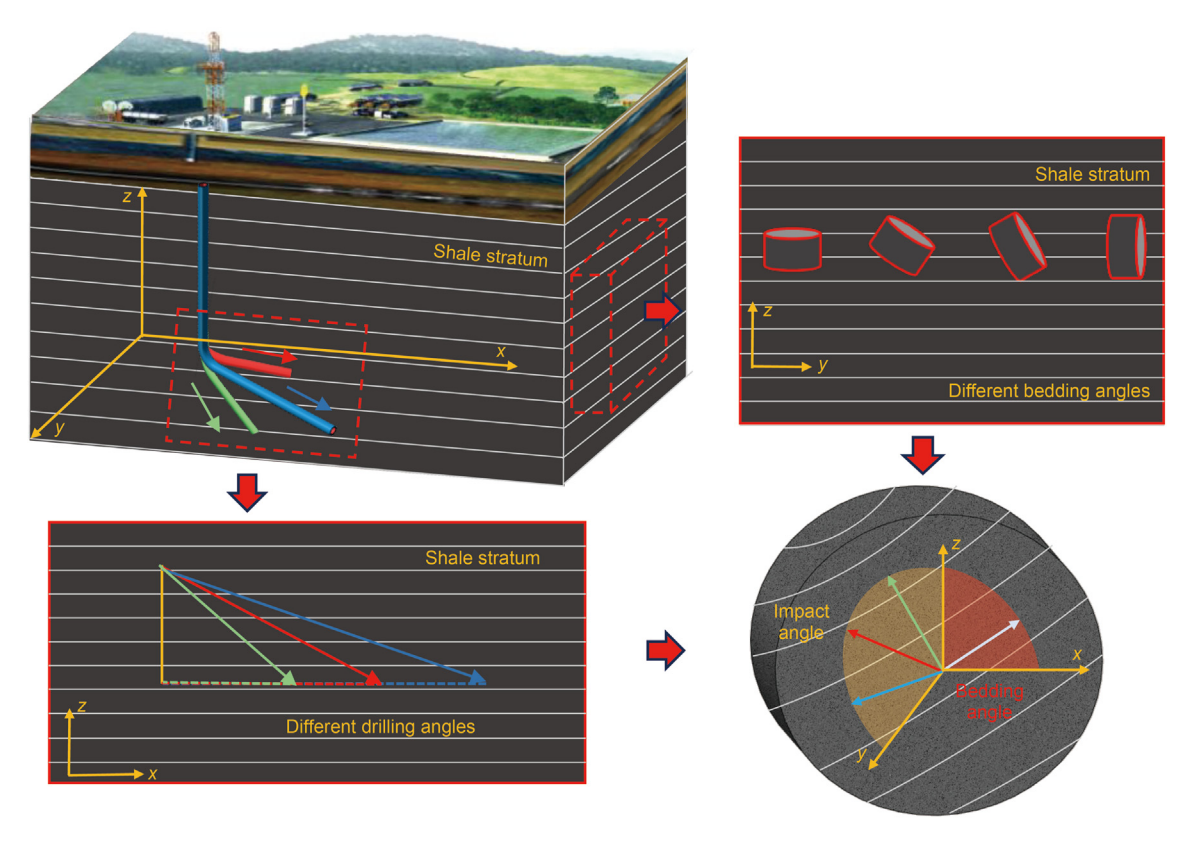


Fig. 1. Schematic diagram of drilling and shale bedding angles.

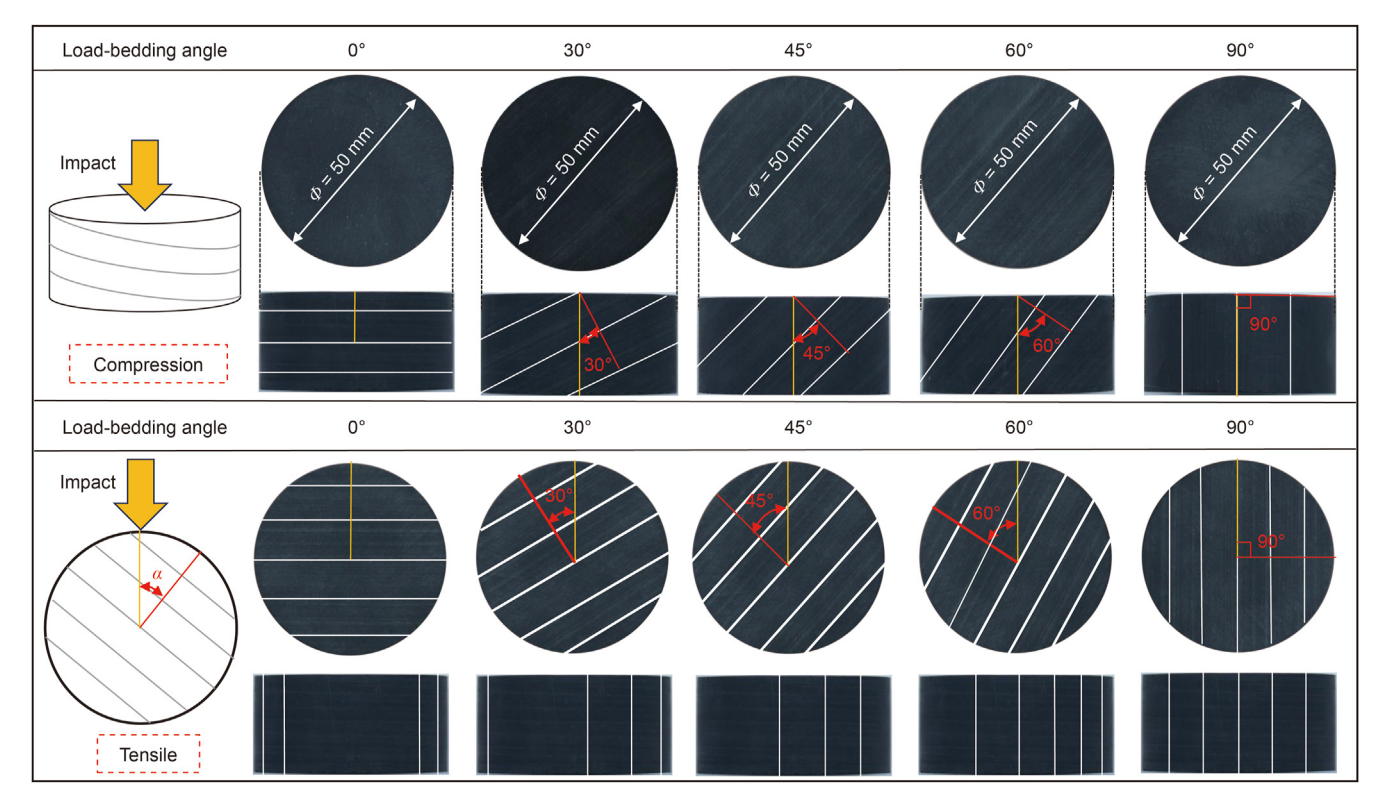


Fig. 2. Schematic diagram of the load-bedding angles of samples.

compressive and tensile failures during the tooth penetration. Rock's dynamic compressive and tensile strengths are essential factors affecting compressive and tensile failures. Additionally, the anisotropy of shale also influences the dynamic compressive and tensile strengths, which should thus be considered during the experimental design and implementation.

(2) The angle between impact load and rock bedding will affect the rock failure characteristics. Horizontal wells are often used in the drilling of deep shale reservoirs. Even if the bedding angle of shale remains unchanged, a certain angle exists between impact load and shale bedding due to the angle between wellbore trajectory and shale bedding, which will also affect the shale fragmentation efficiency of the drill cutter tooth.

As is evident from the above engineering practice, the influence of the law of shale bedding angle on rock dynamics should be considered during research. The rock fragmentation at an angle between impact load and shale bedding should be analyzed. This can provide a basis for investigating the compatibility among impact load, cutter tooth, and anisotropic stratum. Thus, the rock dynamics characteristics under different load-bedding angles and the rock-breaking effect of a single tooth were analyzed during the research.

2.1. Shale specimen preparation

Before experimentation, the anisotropic shale in the deep stratum of the Sichuan Basin was sampled. According to Zhou et al.'s suggestion (Zhou et al., 2012) on the size of shale dynamic test samples, the collected shale was processed into standard cylindrical samples with a diameter of 50 mm, a height of 25 mm, and a height-to-diameter ratio of 1:2. After preparation, the sample sections were polished to ensure that the evenness deviation of shale surfaces did not exceed 0.2 mm.

Considering that the anisotropy influence on the dynamic compressive and tensile strengths of rock should be analyzed, the direction of load changed the impact compression and tensile tests. Hence, the angle between the impact load and the average bedding direction was defined as the load-bedding angle (α). Noteworthy was that the shale samples in the impact tensile test were based on the samples with a 90° angle in the compression test, and the load-bedding angle was altered by rotating the samples (see Fig. 2).

According to α (0°, 30°, 45°, 60°, 90°), ninety samples were grouped (n=18 per group) for impact compression and tensile tests, as displayed in Fig. 3. Meanwhile, considering that the hammer movement velocity in percussion drill during actual engineering ranged between 4 and 9 m/s, and regarding Li et al.'s study (Li et al., 2005) on dynamic impact test, the samples were impacted at velocities of 7.0, 8.0 and 8.5 m/s and, under each impact velocity condition, three samples were used.

2.2. Data processing of the SHPB test

2.2.1. Experimental equipment

To investigate the dynamic properties of shale materials, especially the hale material behavior at high strain rates, an SHPB device was utilized to conduct the impact compression and tensile tests (Zhang et al., 2021). The basic principle of the SHPB test is the process of elastic stress wave propagation in slender rods, which is based on two fundamental assumptions, namely the one-dimensional assumption as well as the assumption of uniformity of stress. The test equipment consisted of a drive system, a pressure bar system, and a signal acquisition and processing system, as

illustrated in Fig. 4.

The spindle impact bar in the drive system could effectively smooth the rising front of the loaded wave, eliminate the high-frequency oscillation of stress wave in the dynamic test, and achieve uniform deformation and dynamic stress equilibrium of specimens during the loading process (Wang et al., 2019; Yang S.Q. et al., 2020). The pressure bar system comprises an incident bar, a transmission bar, and an absorbing bar. The incident and transmission bars were both 50 mm in diameter and 1500 mm in length. They were made of high-strength structural steel alloy with Young's modulus of 210 GPa and 7850 kg/m³ density. Strain gauges were installed in the middle positions to collect strain signals on the bars during the impact process.

The signal acquisition system encompassed a velocity sensor, high-speed camera, and strain meter, of which the camera could take 52,000 photographs within 1 s to analyze the progressive failure process of shale during the transient failure. The strain meter was responsible for collecting the strain signals on the incident and transmission bars based on the calculations of the shale mechanical characteristics under different bedding conditions.

Based on the fulfillment of the above two assumptions, the axial strain rate and strain of samples could be calculated by the following formulas (Wong et al., 2014):

$$\dot{\varepsilon}(t) = \frac{C}{L_s} [\varepsilon_i(t) - \varepsilon_r(t) - \varepsilon_t(t)] \tag{1}$$

$$\varepsilon(t) = \frac{C}{L_s} \int_0^t \dot{\varepsilon}(t) dt = \frac{C}{L_s} \int_0^t [\varepsilon_i(t) - \varepsilon_r(t) - \varepsilon_t(t)] dt$$
 (2)

where C represents the longitudinal wave velocity in the bar (m/s); $L_{\rm S}$ denotes the sample length, m; $\varepsilon_{\rm I}(t)$ $\varepsilon_{\rm T}(t)$ and $\varepsilon_{\rm T}(t)$ respectively indicates the incident, reflected, and transmitted wave strains recorded by the strain gauges (dimensionless).

The loads $F_i(t)$ $F_t(t)$ exerted by the end faces of incident and transmission bars on both sample ends, as well as the stress σ of samples, could be calculated by the following formulas (Zhou et al., 2012):

$$F_{i}(t) = EA[\varepsilon_{i}(t) + \varepsilon_{r}(t)]$$
(3)

$$F_{t}(t) = EA\varepsilon_{t}(t) \tag{4}$$

$$\sigma(t) = \frac{F_i(t) + F_t(t)}{2A_s} = \frac{EA}{2A_s} [\varepsilon_i(t) + \varepsilon_r(t) + \varepsilon_t(t)]$$
 (5)

where E represents the elastic modulus of bars (GPa); A denotes the cross-sectional area of bars (m^2); A_s denotes the sample cross-sectional area (m^2).

2.2.2. Stress equilibrium characteristics

The dynamic stress equilibrium of the SHPB device was crucial and needed to be checked before the compression and tensile tests of the studied shale by the time-history curves of stress wave signals. Given this, stress balance conditions were examined for all the compression and tensile tests with different impact velocities, as depicted in Fig. 5. Clearly, the sum of incident wave signal values and reflected wave signal values was equal to the transmitted wave signal values, indicating that the samples all reached stress equilibrium under different impact velocities (see Fig. 6).

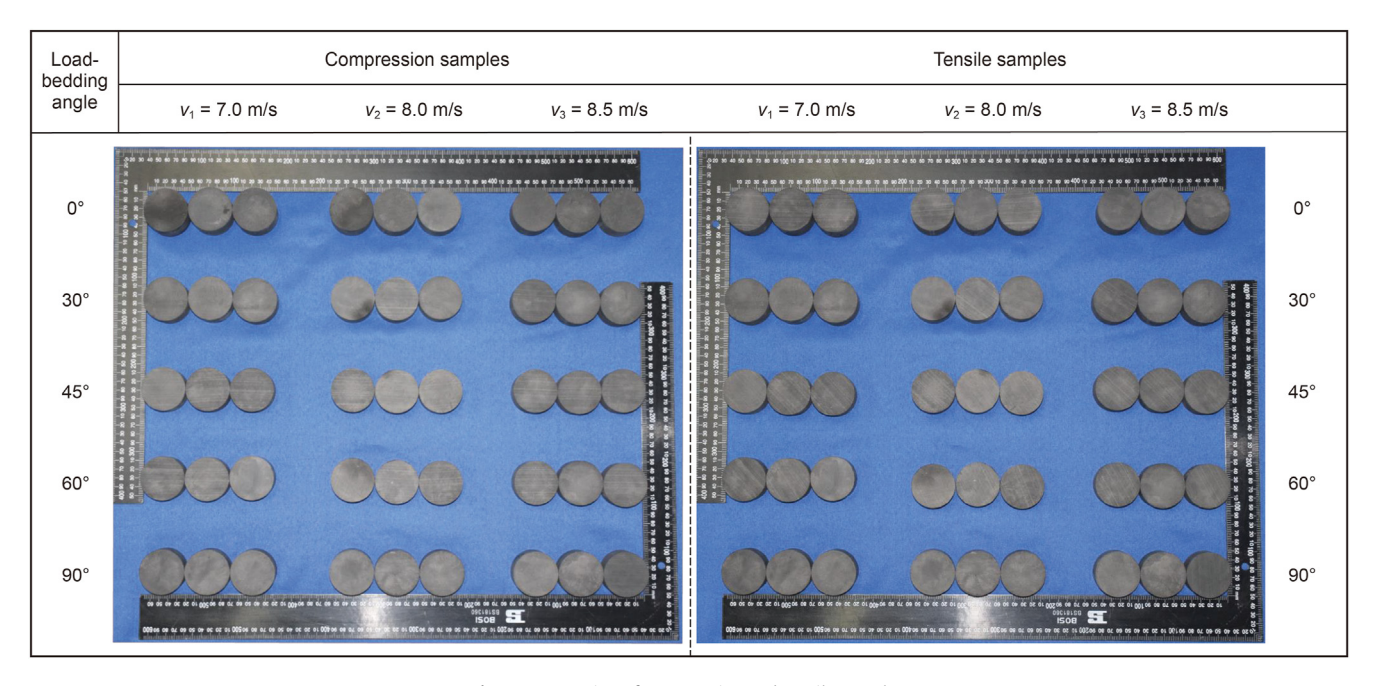


Fig. 3. Preparation of compression and tensile samples.

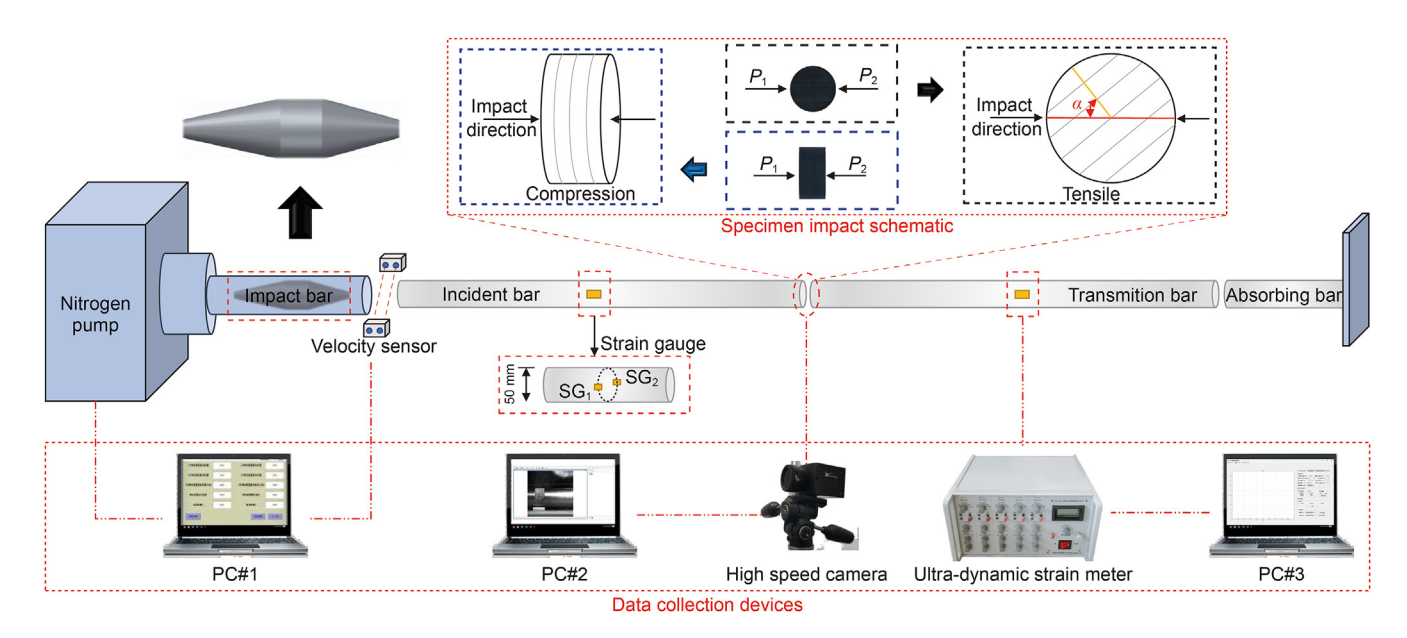


Fig. 4. Schematic diagram of the SHPB experimental system.

2.3. Experimental procedure

Initially, SHPB impact experiments were conducted based on the sample mentioned above grouping at different impact velocities, through which the stress-time curves under impact compression and tensile test conditions were derived. The variations of dynamic compressive and tensile strengths with load-bedding angle during the impact process were analyzed, and the influence of shale anisotropy on the rock dynamic strength was identified.

Next, based on the shooting results of the high-speed camera, the shale failure process under impact load was analyzed, and the failure mechanism under different α was revealed. Meanwhile, the fragmented samples were subjected to fractal dimension analysis

to clarify further the influence law of load-bedding angle on the rock fragmentation.

Finally, the rock-breaking effect of the axe-shaped tooth under different α was analyzed using a single-tooth experimental device under impact load. A 3D scanning device was utilized to measure the volume penetrated by the cutter tooth under the impact load to quantify the rock-breaking effect further. Moreover, the energy absorbed by rock fragmentation during the impact process was calculated, and the influence law of load-bedding angle on the specific energy of rock fragmentation was compared, thereby revealing the rock-breaking mechanism of anisotropic shale under impact load.

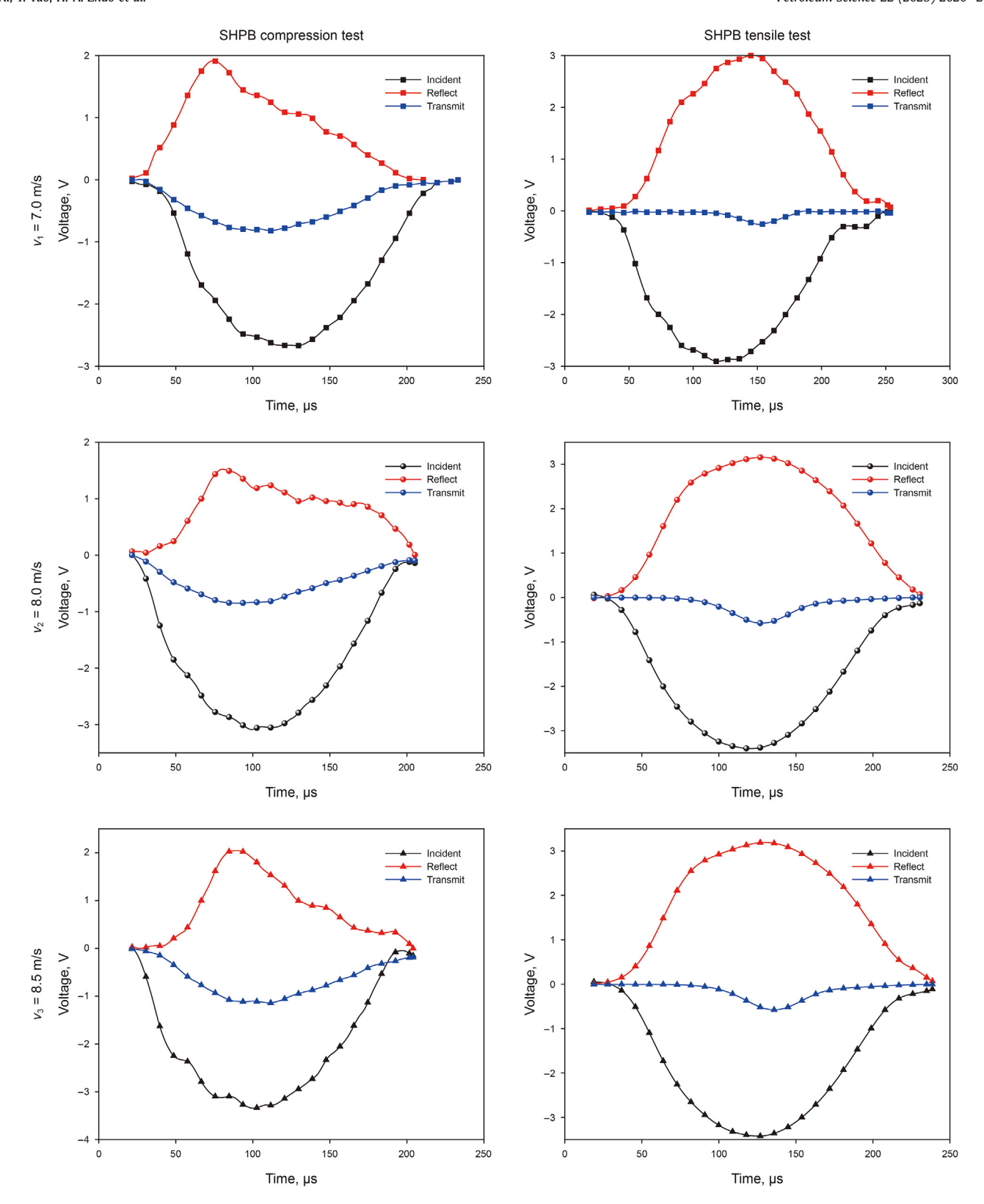


Fig. 5. Dynamic stress equilibrium diagram.

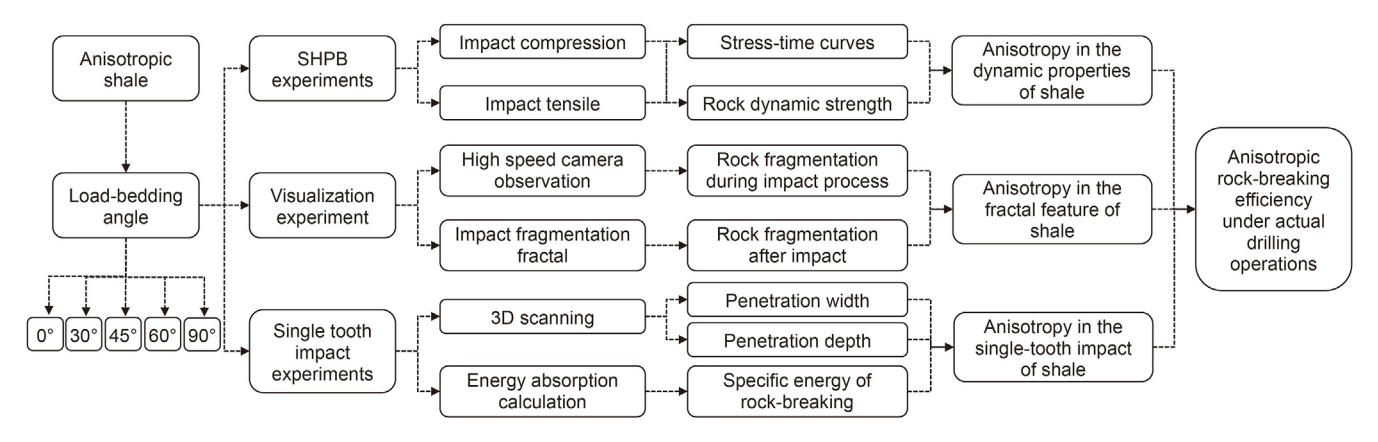


Fig. 6. Dynamic stress equilibrium diagram.

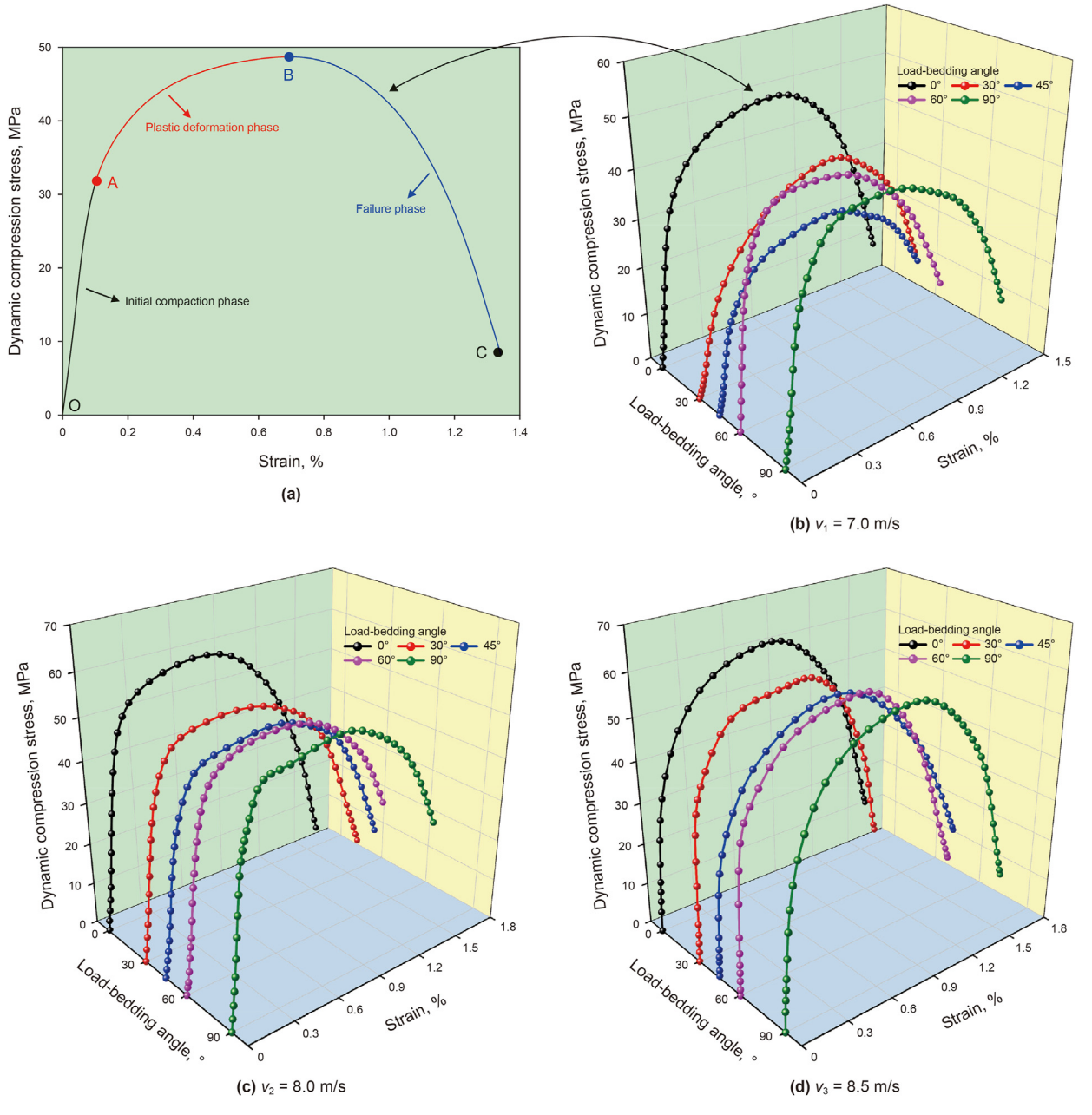


Fig. 7. Dynamic compression stress-strain curves at different impact velocities.

Petroleum Science 22 (2025) 2020-2041

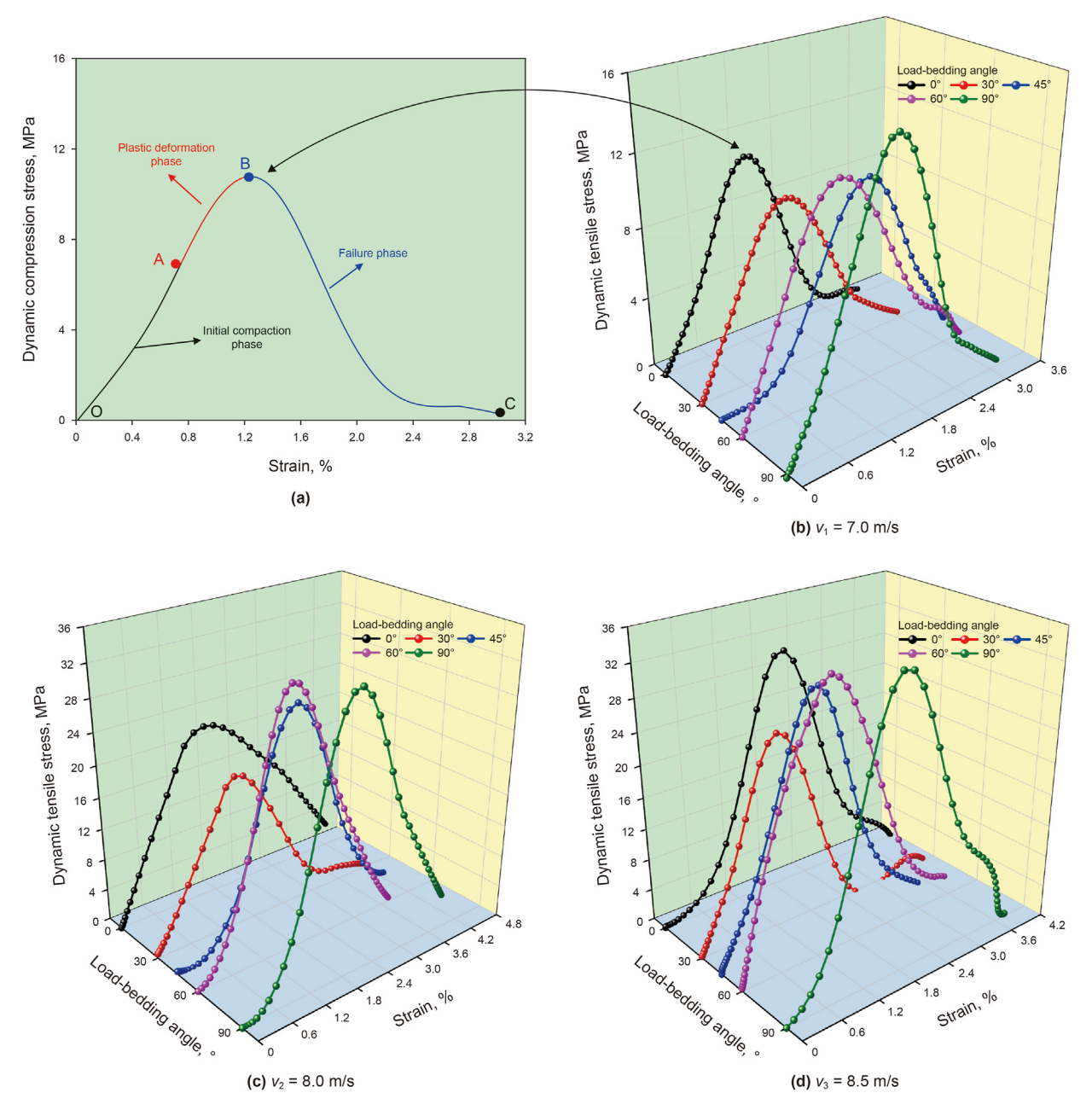


Fig. 8. Dynamic tensile stress-strain curves at different impact velocities.

3. Experimental results

3.1. Variation of rock dynamic strength

3.1.1. Compression and tensile stress-strain curves

As mentioned above, compressive and tensile failures often cooccur during rock fragmentation by impact, and the dynamic compressive and tensile strengths of rock are important indicators reflecting the impact failure (Yin et al., 2012; Xi et al., 2022a). Considering the presence of a noticeable strain rate effect with the rock dynamic strength, that is, the strength of rock changes with the impact velocity, the dynamic compression and tensile stress-strain variations of shales with different α were analyzed under three impact velocities.

Fig. 7 displays shale's dynamic compressive stress-strain curves with different α at various impact velocities.

It is clear from Fig. 7(a) that under impact load, the dynamic compressive stress-strain curves included three phases: initial compaction, plastic deformation, and failure fragmentation. a) Initial compaction phase (corresponding to the OA section of the curves): the samples were in the early stage of loading and still under elastic deformation, during which the pores of shale samples were gradually compacted; b) Plastic deformation phase (corresponding to the section AB of the curves): as the loading progressed, microcracks were formed in the samples, which progressively developed to reach the peak stress gradually; c) Failure phase (corresponding to the section BC of the curves): cracks in the samples would further develop at this phase, leading to a reduction in the overall sample strength and thus a sharp decline in the stress value.

As is evident from Fig. 7(b)–(d), the stress-strain curves underwent changes influenced by different α and impact velocities:

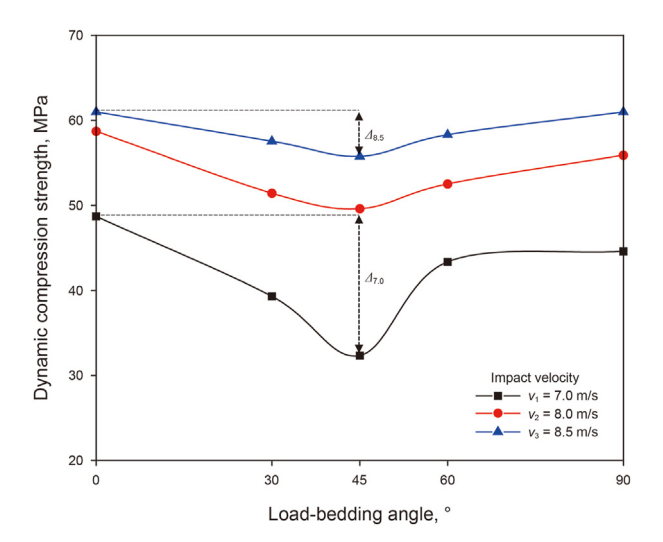


Fig. 9. Dynamic compressive strength of shale under different α .

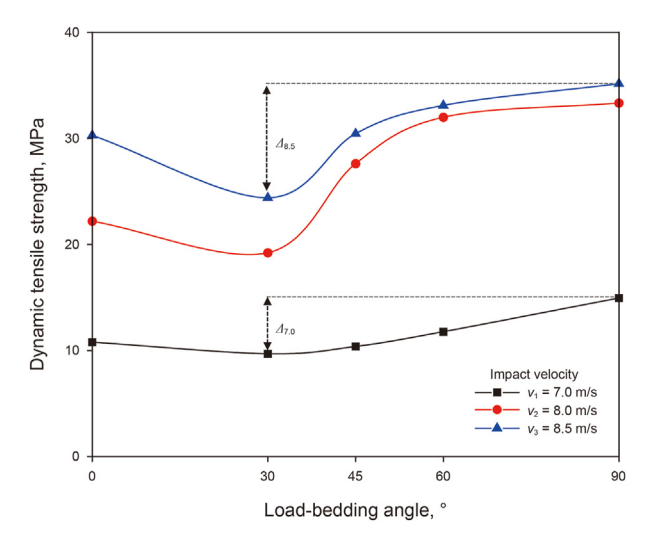


Fig. 10. Dynamic tensile strength of shale under different α .

At the same impact velocities and different α , the peak stress of dynamic compression decreased first and then increased with the continuous increase of α . When $\alpha=45^\circ$, the peak stress was the lowest. At an impact velocity of 7.0 m/s, the peak stress was 48.65 MPa at $\alpha=0^\circ$, whereas it was 32.16 MPa at $\alpha=45^\circ$, showing a decrease of up to 33.90%.

At the same α , the peak stress continued to increase with the elevation of impact velocity. When the impact velocities were 7.0, 8.0 and 8.5 m/s, the peak stresses were 48.65, 58.71, and 61.19 MPa at $\alpha=0^{\circ}$, whereas were 32.16, 49.76, and 55.75 MPa at $\alpha=45^{\circ}$, respectively, showing decreases of 33.90%, 15.24% and 8.89%.

Fig. 8 displays the shale's dynamic tensile stress-strain curves with different α at various impact velocities. As is evident from Fig. 8(a), the dynamic tensile curves could also be divided into three phases: initial compaction, plastic deformation, and failure fragmentation.

According to Fig. 8(b)–(d), the tensile stress-strain curves underwent variations influenced by different α and impact velocities.

(1) At the same impact velocities and different α , the peak dynamic tensile stress decreased first and then increased with the continuous α increase. The peak stress was the lowest at

- $\alpha=30^\circ$, whereas it was the highest at $\alpha=90^\circ$. When the impact velocity was 7.0 m/s, the peak stress was 9.69 MPa at $\alpha=30^\circ$, whereas it was 14.98 MPa at $\alpha=90^\circ$, showing a decrease of up to 35.31%.
- (2) At the same α , the peak stress continued to increase with the increase of impact velocity. When the impact velocities were 7.0, 8.0 and 8.5 m/s, the peak stresses were 9.69, 19.20, and 24.50 MPa at $\alpha=30^\circ$, whereas were 14.98, 33.33, and 35.20 MPa at $\alpha=90^\circ$, respectively, showing decreases of up to 35.31%, 42.39% and 30.40%.

Noteworthy was that compared to the impact compression test, the tangential slopes of the pre-peak stress curves in the stress-strain curves were lower during the impact tensile test, indicating that the shale elastic deformation under tensile action was unobvious, the plastic deformation phase was short, and the failure process was dominated by brittle failure (Zhang et al., 2018; Sha et al., 2020).

3.1.2. Dynamic strength at different load-bedding angles for different impact velocities

Impact velocity and load-bedding angle would simultaneously affect the dynamic strength of the rock (Fan et al., 2021; Wang et al., 2022; Chang et al., 2022). The dynamic compression and tensile strengths were analyzed to analyze further the influence of different α on the dynamic characteristics of shale under impact load.

Fig. 9 depicts the variation law of dynamic compressive strength at different α . As is evident, when α changed from 0° to 90° , the compressive strength first decreased and then increased, presenting a "V"-shaped pattern, with the minimum and maximum strengths found separately at $\alpha=45^\circ$ and $\alpha=0^\circ$, which were similar to the results by Guo et al. (2023). Additionally, at arbitrary α , the dynamic compressive strength continued to increase with the elevation of impact velocity, showing a rather noticeable strain rate effect, which was enhanced first and then attenuated with the increase of α . When $\alpha=45^\circ$, the strength increased most significantly with the elevation of impact velocity.

Noticeably, it can be seen from the figure that α exerted a significant impact on the dynamic compression characteristics of shale, which was constantly weakened with the elevation of impact velocity. When the impact velocities were 7.0 and 8.5 m/s, for instance, the compressive strengths were 48.65 and 61.19 MPa at $\alpha=0^{\circ}$, whereas were 32.16 and 55.75 MPa at $\alpha=45^{\circ}$, respectively, showing differences of $\Delta_{7.0}=16.49$ MPa and $\Delta_{8.5}=5.44$ MPa.

Fig. 10 depicts the variations of dynamic compressive strength with α . As is evident from this figure, when the α changed from 0° to 90° , the dynamic tensile strength of shale decreased first and then increased. The strength value was the lowest when $\alpha=30^\circ$ and highest when $\alpha=90^\circ$. At arbitrary α , the dynamic compressive strength continued to increase with the elevation of impact velocity, revealing a rather noticeable strain rate effect, whose variation was most significant when $\alpha=60^\circ$.

Meanwhile, it is clear from the figure that with the elevation of impact velocity, the influence of α on the dynamic tensile characteristics of shale became increasingly significant. When the impact velocities were 7.0 and 8.5 m/s, for instance, the tensile strengths were 9.69 and 24.50 MPa at $\alpha=30^\circ$, whereas were 14.98 and 35.20 MPa at $\alpha=90^\circ$, respectively, showing differences of $\Delta_{7.0}=5.29$ MPa and $\Delta_{8.5}=20.22$ MPa.

Based on the above results, it could be concluded that α significantly influenced the dynamic strength of shale. With the elevation of impact velocity, the angle influence on compressive strength decreased while that on tensile strength increased.

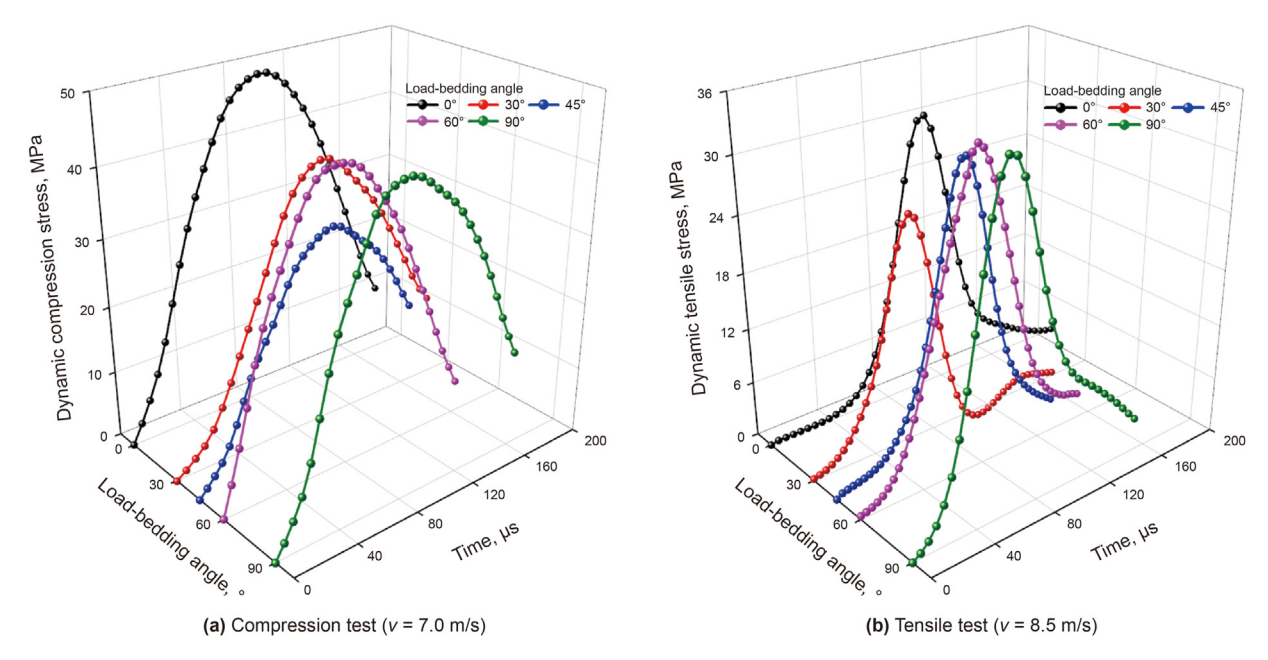


Fig. 11. Dynamic stress-time curves.

3.2. Variation of stress-time curves

To further explore the influence of α on the impact compression and tensile variations under impact load, the dynamic compression stress-time curve at 7.0 m/s impact velocity and the dynamic tensile stress-time curve at 8.5 m/s impact velocity were chosen for analysis, as displayed in Fig. 10.

It is clear from Fig. 11(a) that at an identical impact velocity of 7.0 m/s, the slope of stress-time curves decreased first and then increased with the elevation of α (0°–90°), reaching the minimum when $\alpha=45^\circ$. This indicated that under the influence of α within a 0°–45° range, the deformation resistance of shale and the material's stiffness were gradually weakened.

According to Fig. 11(b), the dynamic tensile stress-time curves presented a similar variation trend at an identical impact velocity of 8.5 m/s. With the elevation of α (0°–90°), the slope of the stress-time curves first decreased and then increased, reaching the minimum when $\alpha=30^\circ$. Suggestively, the tensile failure was most likely to occur at this included angle.

3.3. Morphology of shale fragments under different impact velocities

The size and distribution of rock fragments fractured by impact reflect the failure degree and mode of samples (Feng et al., 2023), while the fragment geometry was closely related to the wellbore cleaning efficiency. Based on this, all rock fragments from dynamic compression and tensile tests were collected to analyze the shale fragmentation under different impact velocities and α , as displayed in Fig. 12(a) and (b).

It is clear from Fig. 12(a) that in the impact compression test, the fragment size of the impacted shale decreased with the elevation of impact velocity at the same α . Under the same impact velocities, i.e., under the same impact energy levels, the number of shale fragments increased first and then decreased with the increase of angle. The number of fragments was the highest when α was 45°, while at 0° and 90°, the number of fragments was smaller and larger.

Fig. 12(b) shows that the impact tensile test's α remained unchanged. At the same time, the fragment size decreased with the

elevation of impact velocity, showing consistency with the aforementioned impact compression test phenomenon. When the impact velocity was constant, the number of fragments increased first and then decreased with the increase of angle. At α of 30°, the number of fragments was the largest, and the fragmentation phenomenon was more prominent.

Based on the above analyses, it could be concluded that α consistently influenced the strength and fragmentation morphology under impact load. This also indicated that compressive failure was more likely to occur when α was 45°, while tensile failure was more likely to happen when the angle was 30°.

4. Discussion

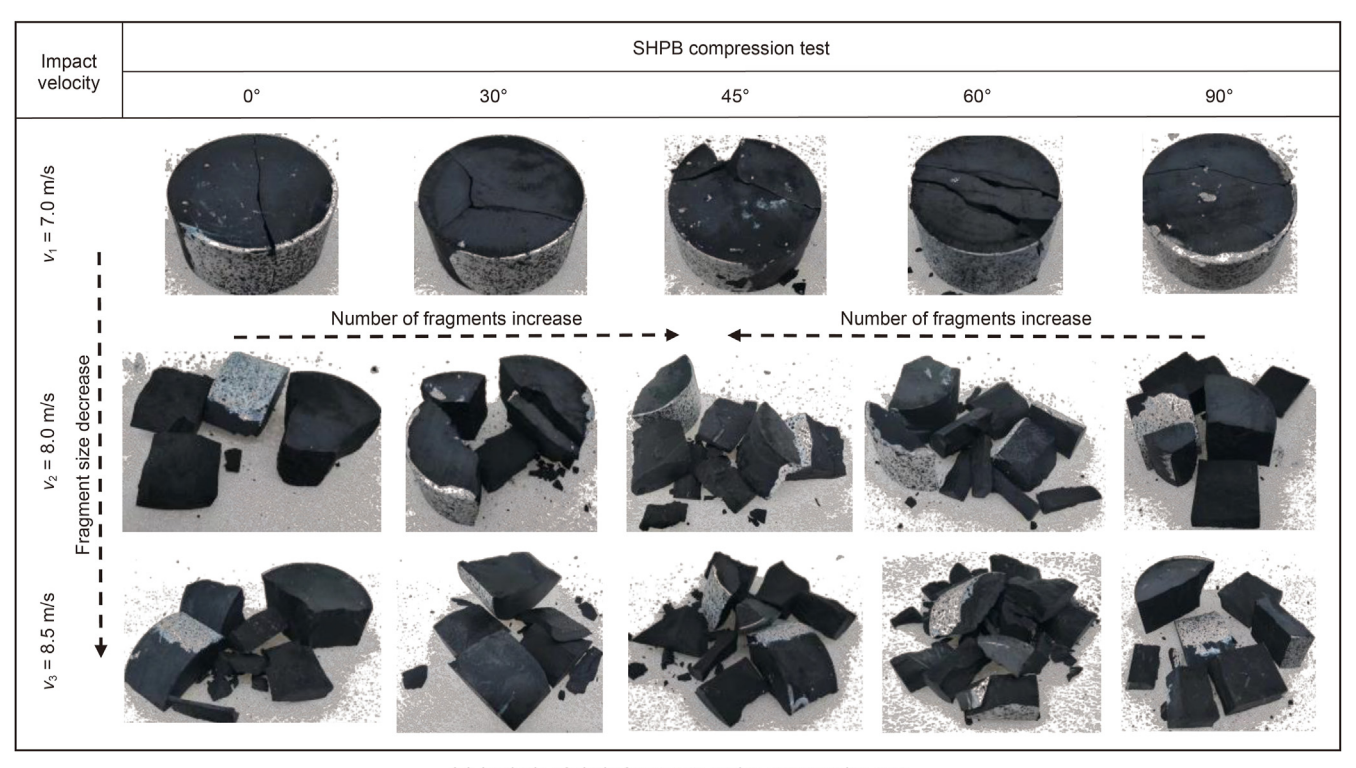
4.1. Analysis of failure mechanism

4.1.1. Analysis of transient failure process

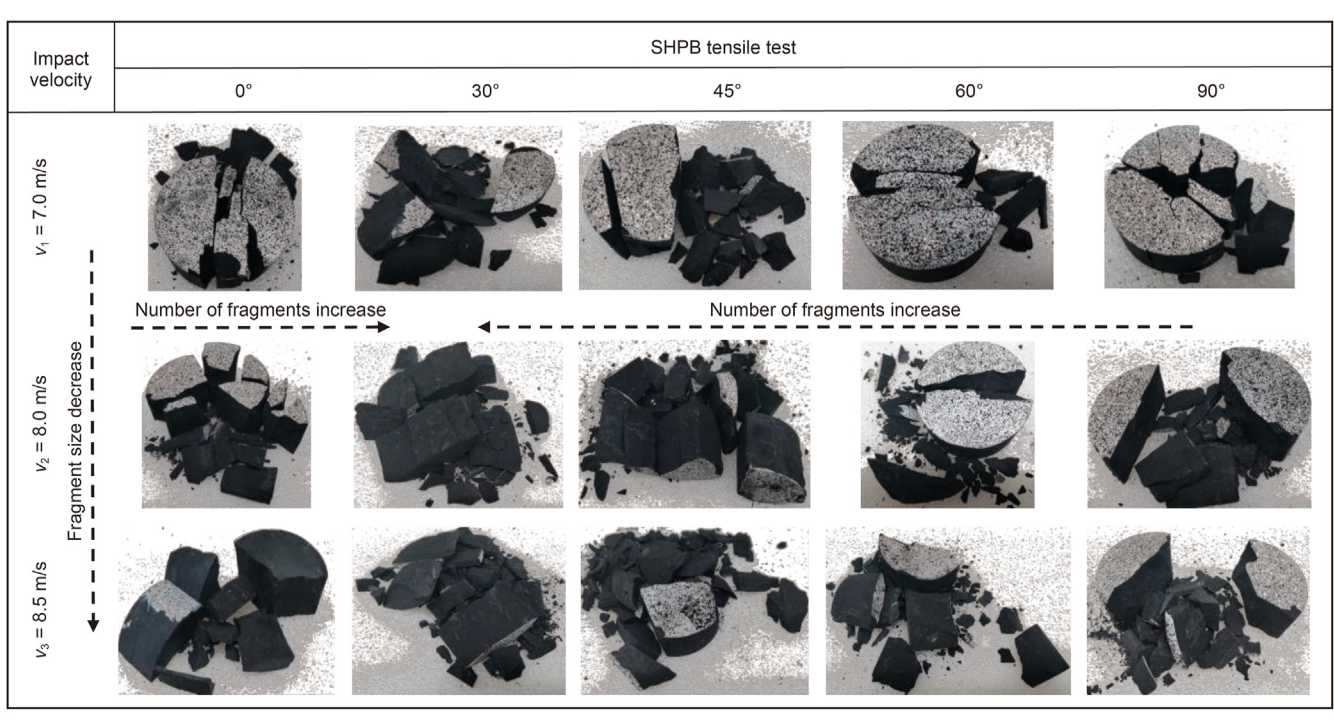
The dynamic failure process of shale under impact load could reveal the influence of α on the fragmentation mechanism. Hence, a high-speed camera was used to photograph the shale failure process with different α in the dynamic compression and tensile tests.

Fig. 13 displays the rocks' dynamic compression failure process under different α , as is evident when $\alpha=0^\circ$ and 90° , the dominant failure mode is an axial failure of samples caused by penetration of impact stress waves through the matrix body and stratification plane. At $\alpha=0^\circ$, tensile failure occurs on the stratification plane in the middle region. At $\alpha=90^\circ$, slight compressive shear failure is present locally. When $\alpha=30^\circ$ and 60° , the cracks are deflected under the influence of bedding, indicating that the weak stratification plane can significantly induce the dynamic fracture propagation path of shale. The effect of laminations on induced crack extension is most pronounced at $\alpha=45^\circ$, leading to crack failure along the delamination plane. This is mainly due to the fact that the stress wave propagates faster than the crack extension, leading to localized compressive shear damage in the sample.

Fig. 14 displays rocks' dynamic tensile failure process at different α . When $\alpha=0^{\circ}$ and 90° , the dominant failure mode is an axial failure of samples caused by penetration of impact stress waves through the stratification plane and matrix body. At $\alpha=0^{\circ}$, the



(a) Analysis of shale fragments under compression test



(b) Analysis of shale fragments under tensile test

Fig. 12. Analysis of shale fragments with different impact velocities.

main crack appears along the central bedding, and tensile failure occurs at the peripheral bedding position. At $\alpha=90^\circ$, apart from generating the main crack along the impact load direction, tensile cracks vertical to the main crack also appear due to bedding perpendicular to the load direction. When $\alpha=30^\circ$, the generated cracks are affected by α , and the crack direction begins to tilt

towards the bedding direction. When $\alpha=45^\circ$ and 60° , the effect of bedding is most significant, resulting in shear failure of cracks along the stratification plane.

4.1.2. Analysis of tensile-compression ratio

Capable of characterizing the brittleness and toughness of

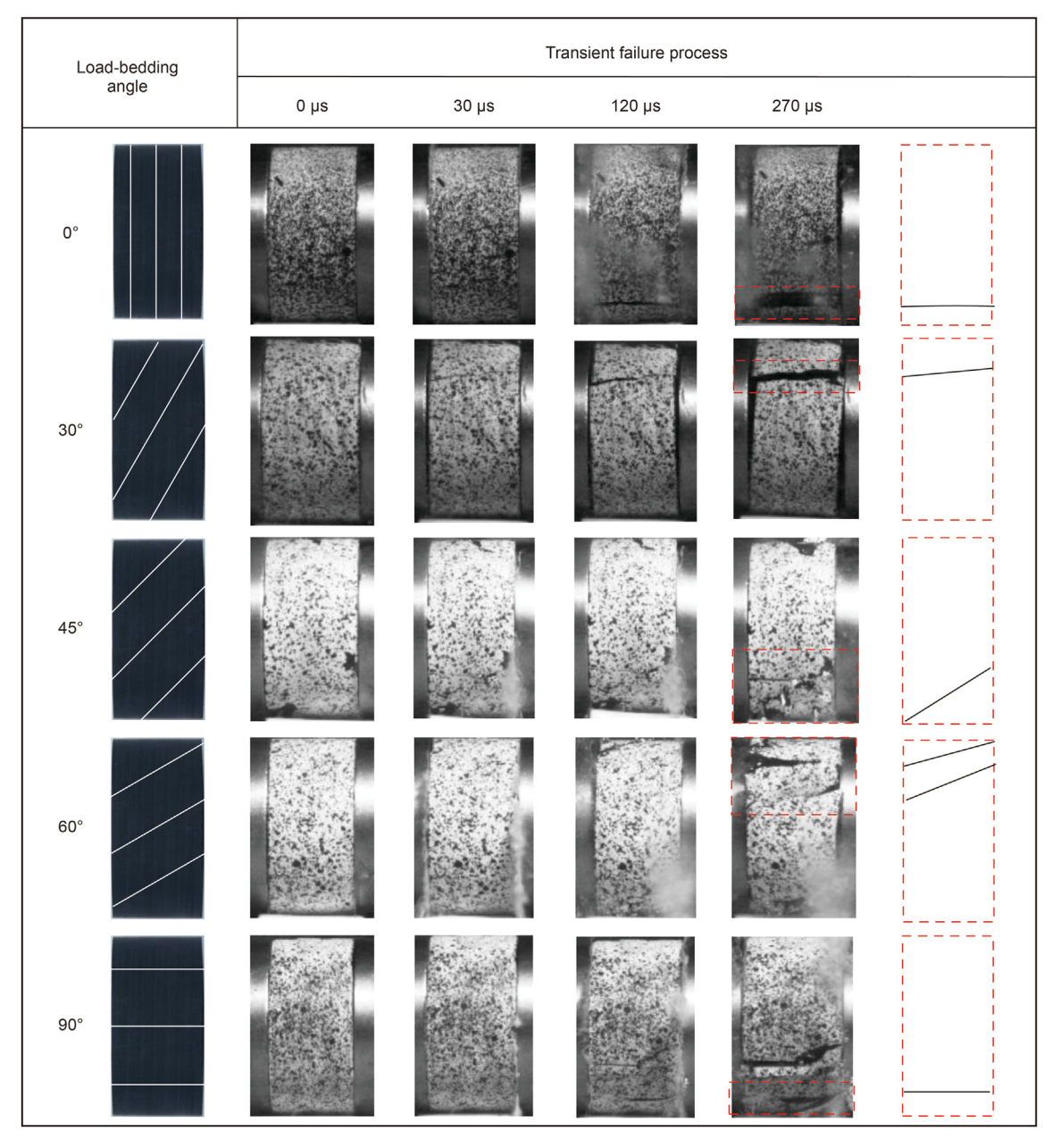


Fig. 13. Analysis of shale compression failure process.

materials, the tensile-compression ratio is closely related to the rock failure characteristics under impact loads (Hucka et al., 1974; Kahraman et al., 2003; Guo et al., 2015). For anisotropic shale, its tensile-compression ratio is also affected by α . The dynamic strength tensile-compression ratio β is introduced to analyze rocks' brittleness and toughness variations under impact load. The specific formula is given in Eq. (6).

$$\beta = \frac{f_{\rm t}}{f_{\rm c}} \tag{6}$$

where f_t denotes the dynamic tensile strength of shale (MPa); f_c indicates the dynamic compressive strength of shale (MPa).

Fig. 15 displays the variation curves of the tensile-compression ratio at different α . As is evident from the figure, α significantly influences the tensile-compression ratio of rock, and such influence becomes increasingly significant with the elevation of impact

velocity. Meanwhile, it is also clear that when α is $30^{\circ}-60^{\circ}$, the tensile-compression ratio changes most drastically.

At a low impact velocity of 7.0 m/s, the tensile-compression ratio first increases then decreases, and later increases again, reaching a maximum of 0.33 when α is 90°. Within an angle range of 30°–60°, the tensile-compression ratio is higher (0.32) at 45°, indicating better toughness of rock at 45° than that at 30° and 60°, which is fully demonstrated by the significant deformation section at the initial deformation position in Fig. 8(a).

When the impact velocity is high (\geq 8.0 m/s), the tensile-compression ratio first decreases and then increases, all of which reach the minimum at α of 30°, showing rather obvious brittleness. When the angle is 30°, the tensile-compression ratio is high, exhibiting relatively high toughness. It is clear from Fig. 12(b) that when α is less than 45°, the rock undergoes rather apparent brittle failure with substantial uniform fragments. When the angle is over

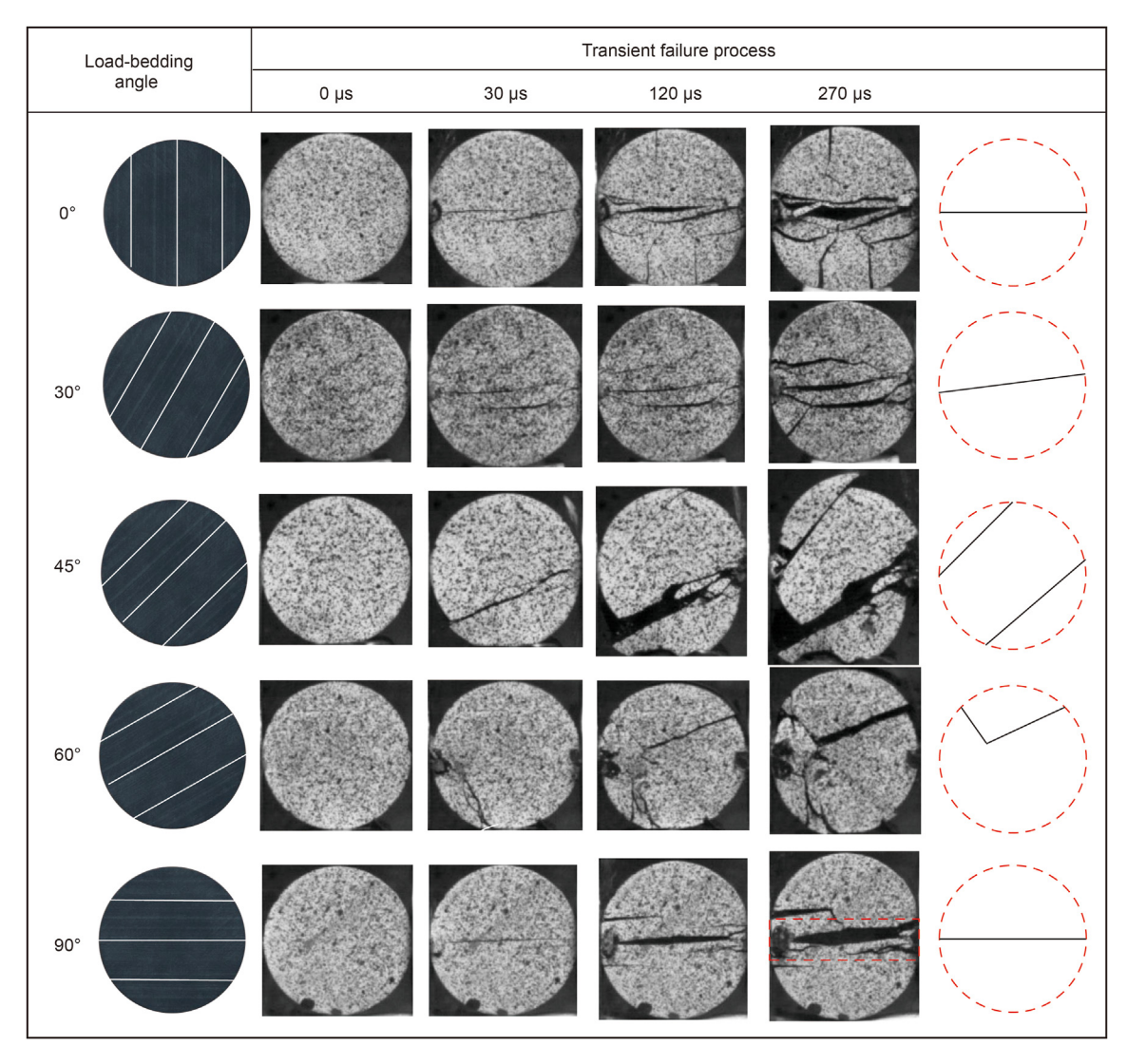


Fig. 14. Analysis of shale tensile failure process.

 60° , the rock experiences alleged ductile failure, breaking into two main blocks and trim fragments.

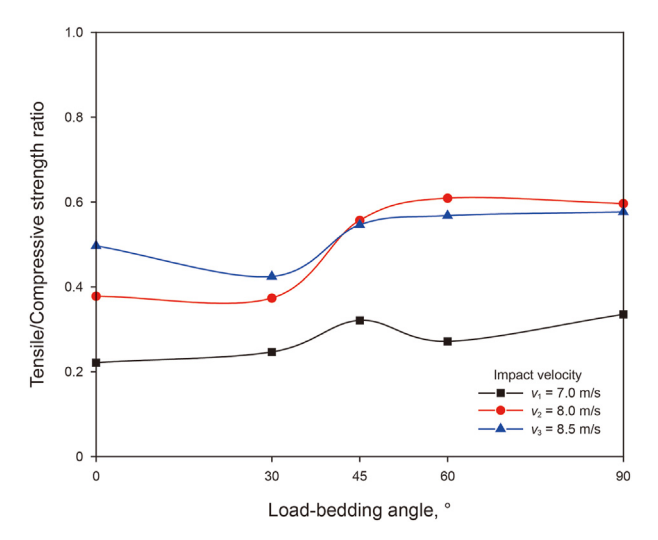


Fig. 15. Dynamic tensile-compression ratio of shale under different α .

4.1.3. Failure mechanism of shale with load-bedding angles

According to the analysis of anisotropic shale failure characteristics, three major failure modes are present for the shale samples with different α : tensile, shear, and mixed failure. The matrix body and stratification plane jointly controlled the crack propagation of samples.

At α of 0° (Fig. 16(a1) and (b1)), the impact load is perpendicular to the stratification plane, and the sample primarily undergoes tensile failure through the stratification plane, with the cracks directly penetrating the matrix body.

When certain α (Fig. 16(a2) and (b2)) is present, the weak bedding plane alters the stress state inside the samples. In this case, shear failure along the stratification direction controlled by the stratification plane primarily occurs, and secondary cracks are generated along the main crack tip. This failure mode most easily produces compressive shear fracture, leading to severe sample failure. This is most significant in the impact tensile and compression tests when α were 30° and 45°.

At α of 90° (Fig. 16(a3) and (b3)), the stress waves are parallel to the stratification plane, and the sample primarily undergoes tensile splitting failure along the stratification plane due to the lower bonding strength of the stratification plane. Under stress waves, mineral grains are more prone to intergranular fracture, and the

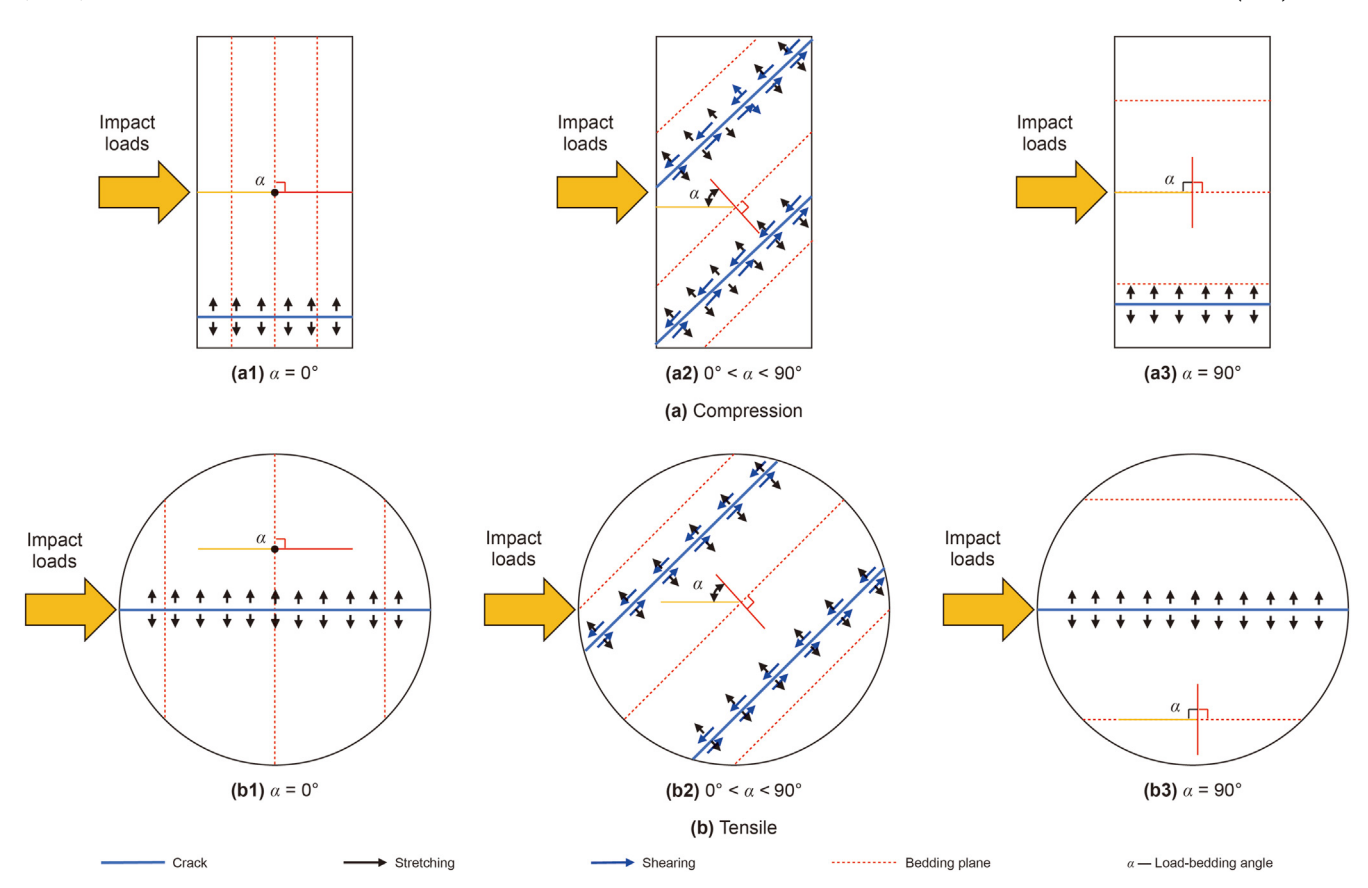


Fig. 16. Failure mechanism of shale under different α .

cracks spread and penetrate along the weak bedding plane, ultimately forming the main crack along the impact load direction.

4.2. Analysis of fractal dimension

4.2.1. Analysis of the degree of fragmentation with load-bedding angles

Due to anisotropy, shale undergoes varying degrees of fragmentation under the same impact conditions. The fragments' geometrical size and fractal characteristics could reflect the absorption of impact load energy by shales with different α . This could provide the basis for compatibility analysis of impact load and rockbreaking effect. Hence, in this study, rock fragments are filtered through screens with aperture diameters of 0.15, 0.30, 0.60, 1.20, 2.40, 4.80, and 9.60 mm, and the size and mass of fragments are quantified, thereby analyzing the influence law of α on the degree of rock fragmentation under different impact velocities.

Figs. 17 and 18 depict the correlation between fragment mass and size during the failure of shales with different α in the impact compression and tensile tests, i.e., the cloud diagrams of correlation between the cumulative mass of fragments and the mesh size less than a particular value. Different color scales represent the mass ratios of fragments of various sizes to the corresponding samples.

Fig. 17(a), (b), and (c) illustrate the cumulative mass variations of fragments of different sizes under different α at 7.0, 8.0, and 8.5 m/s impact velocities during the impact compression test, respectively. As is evident, with the elevation of impact velocity, the mass of rock fragments formed by shale impact increases gradually. At the same impact velocities, the cumulative mass of fragments reaches the maximum when $\alpha=45^{\circ}.$

At a 7.0 m/s impact velocity, although the impacted shale could

fracture, the generated fragments are large in size and small in number. When $\alpha=45^\circ,$ the number of fragments is the largest, accounting only for 0.53% of the total sample mass. With the elevation of impact velocity (8.5 m/s), the mass of fragments increases significantly, with those generated at $\alpha=45^\circ$ accounting for 17.8% of the total sample mass.

Fig. 18(a), (b), and (c) illustrate the cumulative mass variations of fragments of different sizes under different impact velocities and α in the impact tensile test. As is clear, the fragmentation of shale under tensile failure is more severe than that under compression at the same impact velocities. α significantly influences the generation of fragments, and the cumulative mass of fragments is the largest when $\alpha=30^\circ$. At impact velocities of 7.0, 8.0, and 8.5 m/s, the cumulative mass of rock fragments accounts for 18.79%, 22.78%, and 34.71% of the total sample mass when $\alpha=30^\circ$.

4.2.2. Analysis of fractal dimension with load-bedding angles

To further quantify the degree of rock fragmentation under impact load, fractal dimension D was used to quantify the size distribution of shale fragments.

During the analysis, the degree of shale fragmentation is evaluated first by the average size of fragments, as described in Eq. (7) (Deshpande and Chakraborty, 2023; Zhao et al., 2023):

$$\overline{d} = \frac{\sum d_i M_i}{M} \tag{7}$$

where \overline{d} represents the average particle size of sample fragments, mm; d_i represents the average fragment size between two screen aperture sizes, mm; M_i denotes the mass of fragments in the screen with aperture d_i , g; M denotes the total mass of fragments, g.

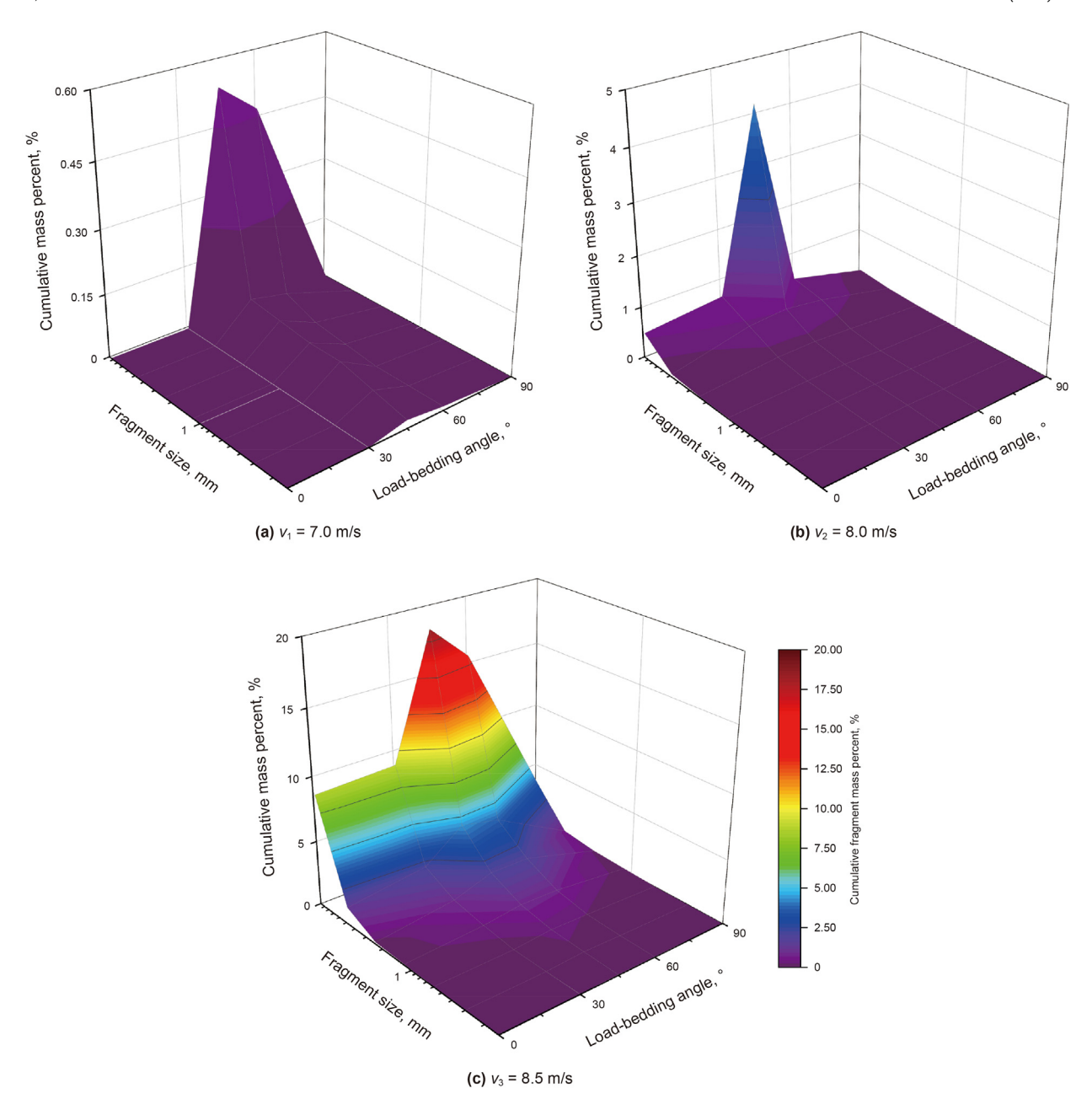


Fig. 17. Surface diagrams for correlation between fragment size and mass of compression samples.

Meanwhile, the dynamic fragmentation of rocks is statistically explored based on the distribution of fractal dimension *D*, and the size of fragments could be characterized by the power law relationship (Turcotte, 1986). The *D* value of shale during dynamic stretching is calculated according to Eq. (8):

$$y_i = \frac{M(d_i)}{M} = \left(\frac{d_i}{d_{\text{max}}}\right)^{3-D} \tag{8}$$

where $M(d_i)$ represents the cumulative mass of fragments smaller than d_i , and d_{max} denotes the maximum fragment size.

Data points are linearly fitted by taking logarithms on both sides of Eq. (8) using the least squares regression. The fractal dimension D is derived from the linearly fitted straight slope equal to 3-D.

Considering that the fracture characteristics of samples are more evident under the impact tensile condition, the fractal dimension variation of samples is analyzed under this condition, as displayed in Fig. 19, at impact velocities of 7, 8.0 and 8.5 m/s, the slope of the fitting curve is the smallest when $\alpha=30^\circ$, indicating that the D value at 30° was the largest and that the fragmentation of rocks is most significant under this condition.

4.3. Analysis of single-tooth penetration effect

In actual drilling engineering, when a drill bit breaks rock under impact load, it is necessary to consider the impact parameters and formation anisotropy characteristics and the influence of the bit tooth on the rock-breaking effect (Xi et al., 2022b). Given this, the single-tooth impact test is conducted with a PDC bit single-tooth device, and the changes in tooth penetration depth and rock-breaking volume during the impact process are analyzed under different α , thereby quantitatively evaluating the influence of

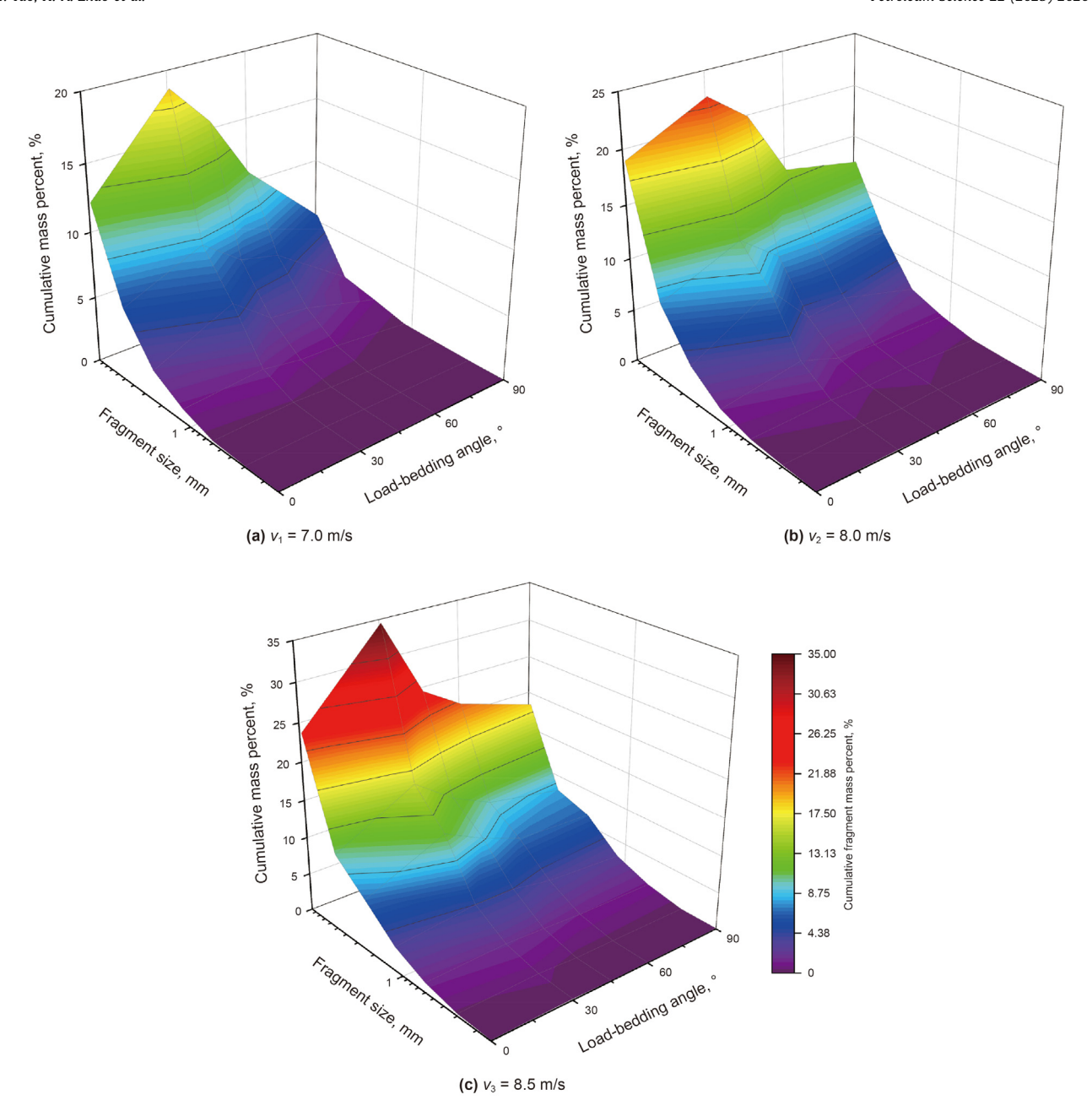


Fig. 18. Surface diagrams for correlation between fragment size and mass of tensile samples.

impact load on the improvement of rock-breaking efficiency.

4.3.1. Axe-shaped tooth penetration effect

During the test, the axe-shaped tooth is adopted for impact fragmentation, as displayed in Fig. 20. Its rock-breaking mechanism is that when the tooth edge contacts the rock, a shear stress concentration zone is formed inside the rock, making the rock more prone to shear failure, thus facilitating the rock fragmentation. As the tooth edge penetrates deeper into the rock, the ridge of the tooth wedges into the rock, resulting in lateral tensile failure of the rock. Given the axe-shaped tooth's peculiar design and rock-breaking mechanism, it is not susceptible to impact failure when used in downhole applications, thus having a longer service life.

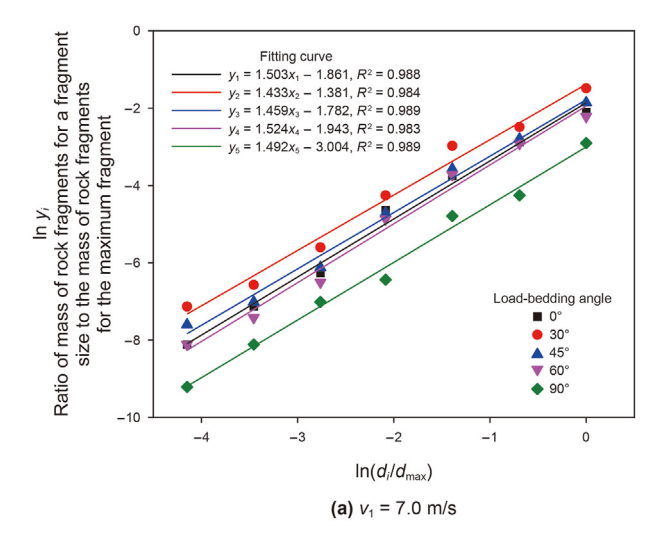
To ensure that the drill tooth penetrates the rock during the test and that the rock is not completely fragmented, the test is conducted at an impact velocity of 5.0 m/s by taking into account the

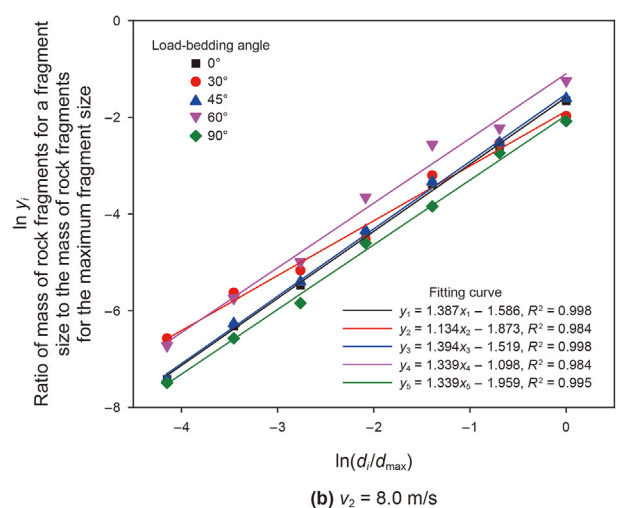
afore-described SHPB impact test effect and a 4-9~m/s movement velocity range of percussion drill hammer adopted in the actual engineering.

After the impact of shales with different α by drill cutter tooth, a 3D scanning device is used to measure and analyze the generated impact pits, and the results are detailed in Fig. 21.

As is evident from the above figure, during the rock penetration by the drill cutter tooth under impact load, "impact pits" corresponding to the tooth's shape are generated. Influenced by α , the depth and width of the impact pits change significantly, as depicted in Fig. 22.

When $\alpha=45^\circ$, the penetration depth of the drill cutter tooth is the greatest (10.1 mm), primarily because the dynamic compressive strength is the lowest under this condition. According to the aforedescribed tooth—rock interaction mechanism, the penetration depth is mainly affected by the compression failure. Considering





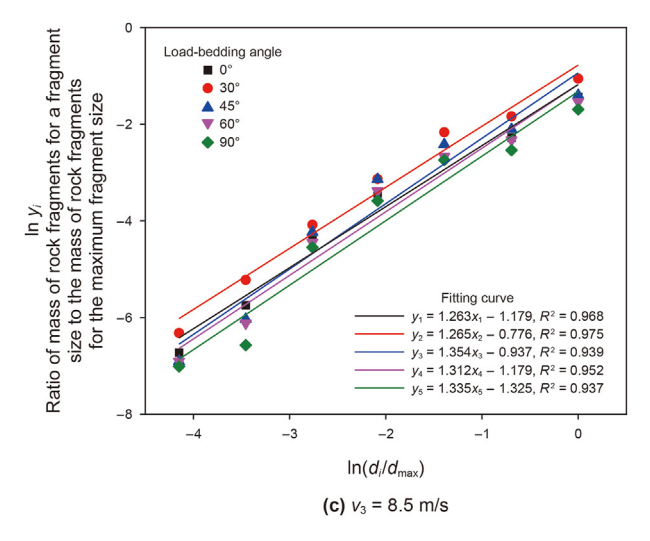


Fig. 19. Fractal dimension determination of the samples (tensile).

that the dynamic compression strength of shale is the lowest at this angle, the depth generated during penetration is the greatest.

When $\alpha=30^\circ$, the width of the impact pit generated by the drill cutter tooth is the greatest (24 mm), primarily because the tensile strength of the rock is the lowest under this condition. The ridge

shape of the axe-shaped tooth would wedge into the rock, causing lateral tensile failure of the rock, resulting in the formation of an impact pit with a certain width. Considering that the dynamic tensile strength of the rock is the lowest at this angle, the generated impact pit was the widest.

4.3.2. Calculation of rock-breaking specific work

Since rock dissipates and absorbs energy during impact fragmentation, analyzing energy changes in the impact process helps improve rock-breaking efficiency (Wang et al., 2017). Meanwhile, the rock's energy absorption efficiency directly affects the drill bit's rock-cutting and breaking effects. Under the same impact energy levels, rocks with high energy absorption efficiency are more prone to fracture, thus accelerating the drilling speed and improving the drilling efficiency (Han et al., 2020). The energies and energy absorption efficiency of rock are calculated by the following formulas (Xi et al., 2023):

$$W_{\rm I}(t) = (A_0 C_0 / E_0) \int \sigma_{\rm I}^2(t) dt$$
 (9)

$$W_{R}(t) = (A_{0}C_{0}/E_{0}) \int \sigma_{R}^{2}(t)dt$$
 (10)

$$W_{\rm T}(t) = (A_0 C_0 / E_0) \int \sigma_{\rm T}^2(t) dt$$
 (11)

where $W_{\rm I}(t)$, $W_{\rm R}(t)$, and $W_{\rm T}(t)$ respectively represent the incident energy, reflected energy, and transmitted energy (J); $\sigma_{\rm I}(t)$, $\sigma_{\rm R}(t)$, and $\sigma_{\rm T}(t)$ respectively represent the amplitudes of the incident, reflected and transmitted stresses at time t (MPa); A_0 , C_0 , and E_0 respectively denote the cross-sectional area (mm²), longitudinal wave velocity (m/s) and elastic modulus (GPa) of the incident and transmission bars in the SHPB test.

According to the law of conservation of energy, the absorbed energy $W_A(t)$ of the rock samples in the test was calculated according to Eq. (12) (Han et al., 2020):

$$W_{\rm A}(t) = W_{\rm I}(t) - W_{\rm R}(t) - W_{\rm T}(t)$$
 (12)

The energy absorption efficiency α of rock was calculated as follows:

$$\alpha = W_{\mathsf{A}}(t)/W_{\mathsf{I}}(t) \tag{13}$$

Based on the above formulas, the absorbed energy and energy absorption efficiency of rock during fragmentation by cutter tooth is calculated under different α , as depicted in Fig. 23. As is clear, the energy absorption efficiency of anisotropic shale was the highest when $\alpha=45^{\circ}$.

To further analyze the rock-breaking effect of energy exerted on the rock by impact load, in addition to the crack width, depth, and energy absorption efficiency measure above, the rock-breaking specific work η at each α should also be calculated, which served as the evaluation standard for the rock-breaking effect of shales with different α :

$$\eta = \frac{W_{\mathbf{A}}(t)}{V} \tag{14}$$

where *V* represents the volume of impact pit generated after rock breakage, cm³; η denotes the rock-breaking specific work, J/cm³.

A 3D scanner is used to scan and calculate the volume at the fragmented site, and the relation curve for rock-breaking specific work of shale under different α is derived as depicted in Fig. 24. As is clear, the particular work values vary greatly by α , and the

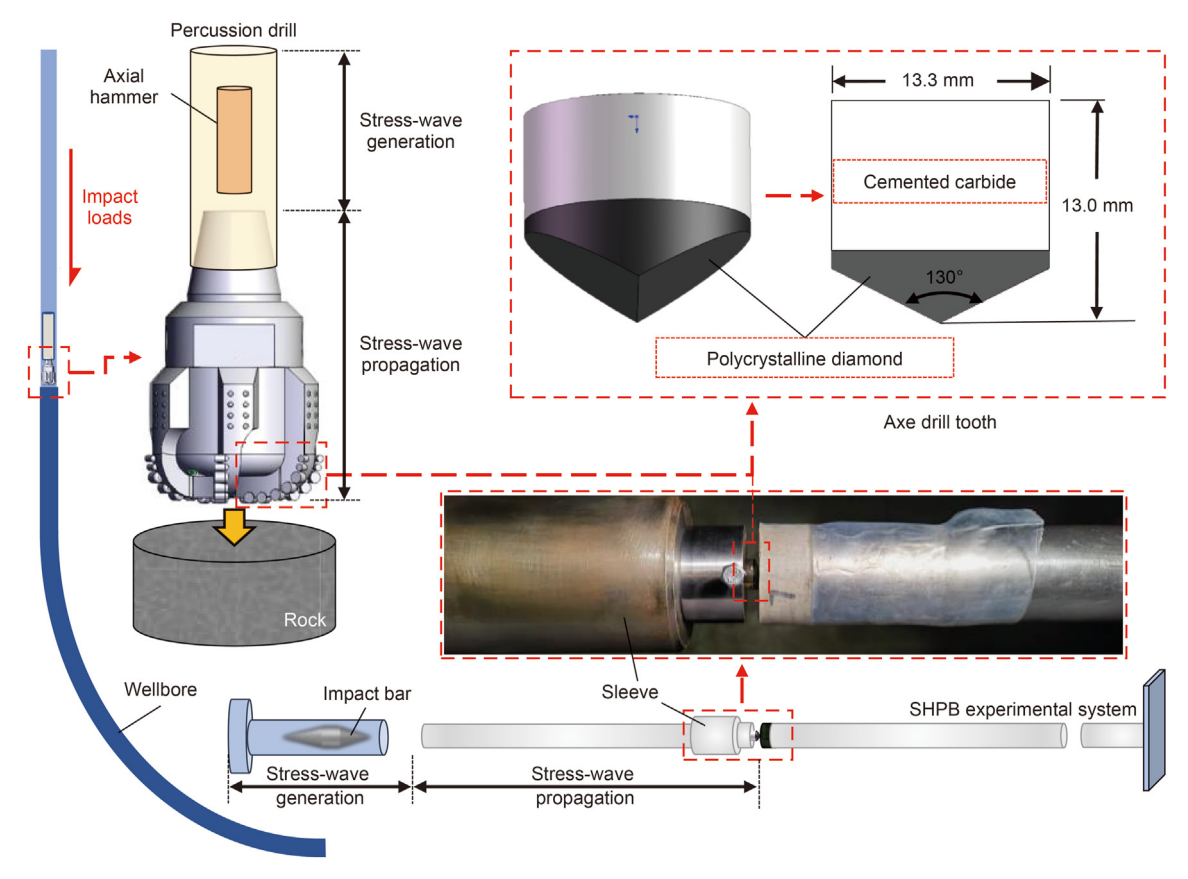


Fig. 20. Photograph and schematic of axe-shaped tooth structure.

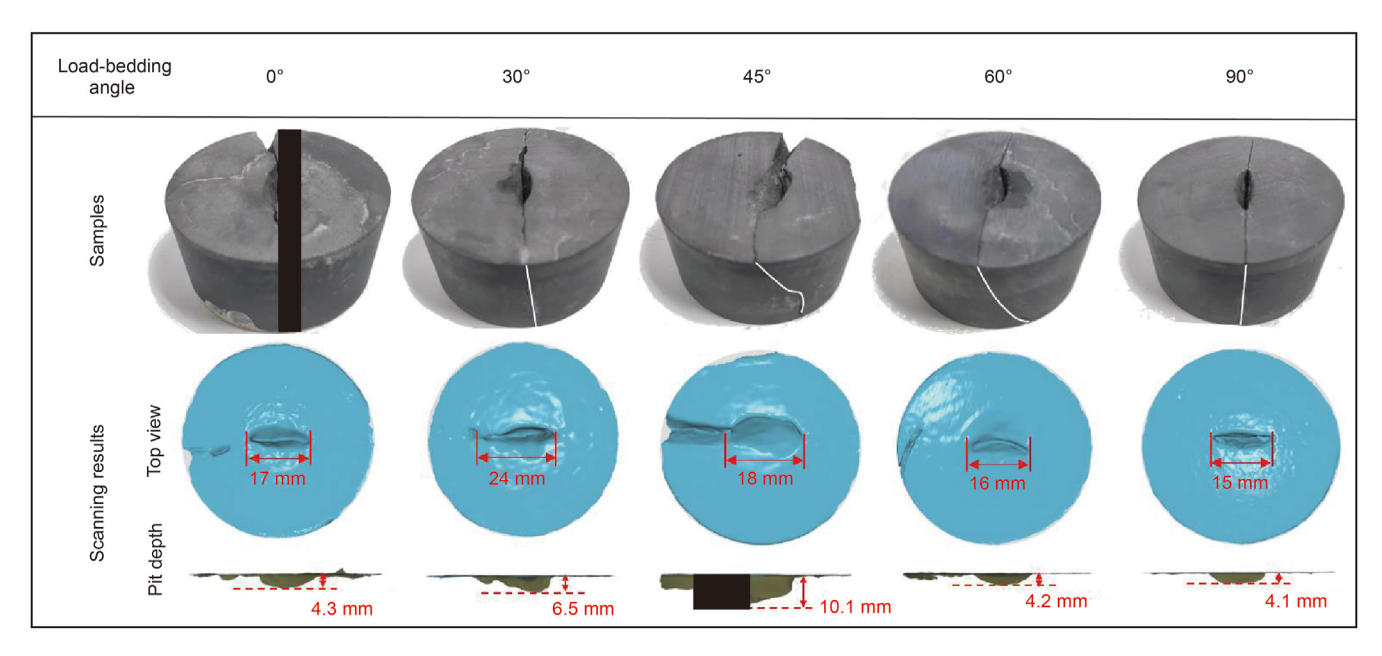


Fig. 21. Shale samples and scanned images after single-tooth impact.

anisotropy performance is strong. When α is 30° , the specific energy is the least, suggesting that the least energy is consumed to achieve the same rock fragmentation effect. Contrastively, to attain the same effect at α of 90° , the energy absorption requirement is nearly five times that of the former.

4.3.3. Rock-breaking mechanism under different load-bedding angles

Based on the above analysis, α significantly influences the rock-breaking effect during the rock-breakage with PDC bit single tooth in a deep shale reservoir. Combining the experimental results concerning the influence of loading-bedding angle on the rock

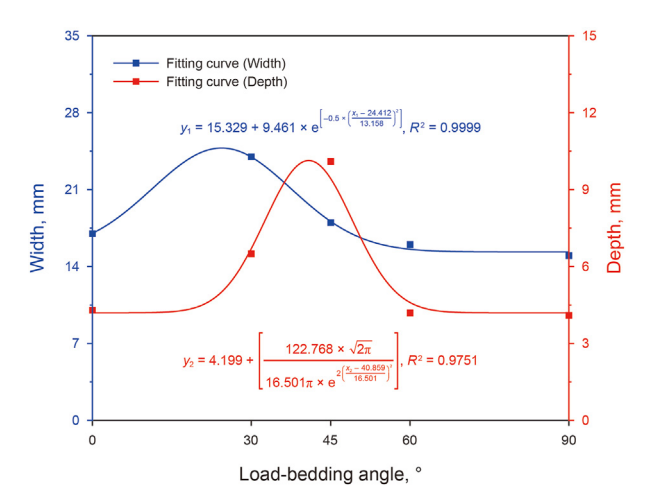


Fig. 22. Width and depth of cracks under impact load.

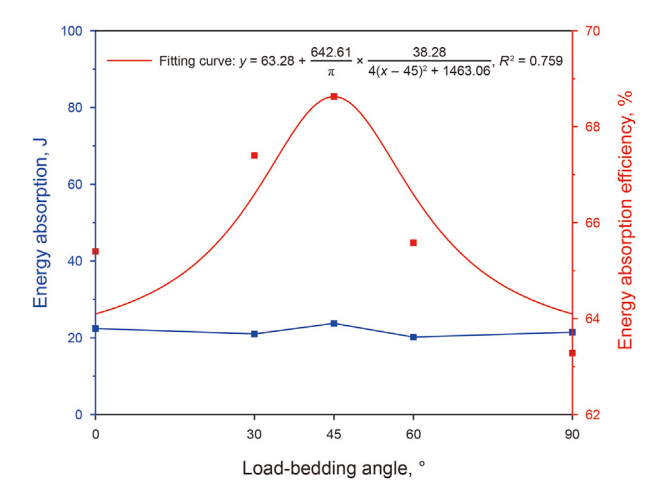


Fig. 23. Energy absorption and energy absorption efficiency of shales with different α .

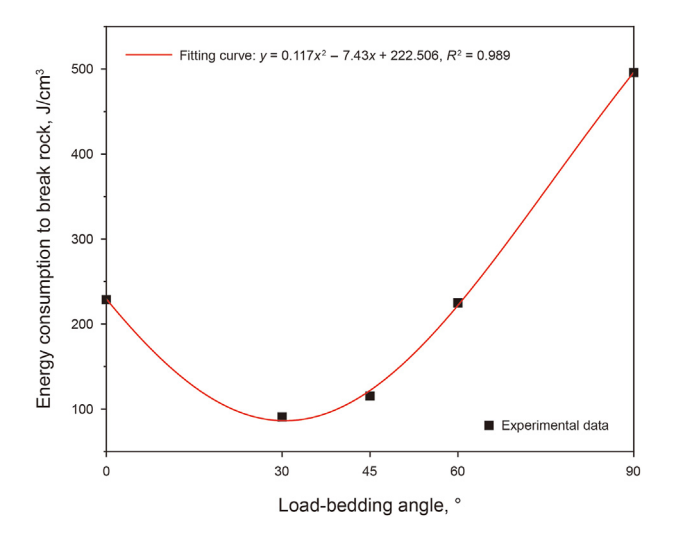


Fig. 24. Energy consumption to break shale under different α .

dynamic properties, the rock-breaking mechanism of anisotropic shale by the axe-shaped tooth is analyzed.

Firstly, for isotropic rocks, the rock-breaking process by axe-

shaped tooth could be divided into the following three phases (Fig. 24).

I: During the rock penetration by the axe-shaped tooth, the tooth edge contacts the rock, beginning to impose the compressive stress $\sigma_{\rm C}$ on it. The rock interior along the tooth edge angle direction is subjected mainly to the compressive stress from the axe-shaped tooth, forming a rather obvious compressive stress zone in front of the cutting tooth.

II: When the axe-shaped tooth penetrates the shale forward, both sides of the tooth edge contact the shale, and the axe-shaped tooth produces the shearing stress $\sigma_{\rm S}$ on the shale. With the deepening of the penetration, the shear cracks extend rapidly and propagate towards the free surface of shale, producing large-volume fragmentation.

III: As the tooth edge gradually penetrates deeper into the rock, the ridge of the axe-shaped tooth wedged into the rock, and both tooth sides are pressed to produce tensile stress $\sigma_{\rm t}$, resulting in lateral tensile failure of the rock.

When the wellbore trajectory passes through the anisotropic shale, α at different trajectories varies. Hence, the anisotropic shale fragmenting effect of the axe-shaped tooth also varies at other positions, as displayed in Fig. 25.

- (1) When the drill bit is in the vertical well section, the dynamic load generated by the percussion drill is transmitted to the cutter tooth to act on the horizontal stratified rock directly (see Fig. 26). At this time, α is 0°. As is evident from the above analysis, the rock's dynamic compressive and tensile strengths are high under this condition, the depth of tooth penetration is d_0 , and the width of the formed impact pit is l_0 .
- (2) As the drill bit gradually enters the inclined well section, α increases. When the angle increases to 30°, the tensile strength of shale is the lowest based on the above analysis. Combined with the afore-described rock-breaking mechanism by axe-shaped tooth, the influence of α at this time is primarily reflected in the phase III of rock breakage. Under the same impact loads, the dynamic tensile strength is relatively low, so the range of tensile failure was more extensive, resulting in a larger range of rock breakage by the drill cutter tooth ($l_{30} > l_0$).

With the deepening of drill bit penetration, α continues to increase. At an angle of 45°, the dynamic compressive strength of rock is the lowest. Based on the above analysis, the influence of α at this time is primarily reflected in the phase II of rock breakage. Under the same impact loads, the dynamic tensile strength is relatively low so that the penetration depth would be deeper $(d_{30} > d_0)$, the penetration rate would increase, and the possibility of bit jumping.

(3) When the drill bit is in the horizontal bedding section, α reaches 90°. Based on the above analysis, the rock's dynamic compressive and tensile strengths reach the highest under this condition, and the tensile-compression ratio is relatively high, efficiently producing plastic failure. Hence, the rock's damage range and penetration depth are the least under this condition ($l_0 > l_{90}$ and $d_0 > d_{90}$).

5. Conclusion

Dynamic property tests and single-tooth rock-breaking tests of anisotropic shale are conducted under impact loads to investigate the failure mode, fractal dimension, and specific work performed

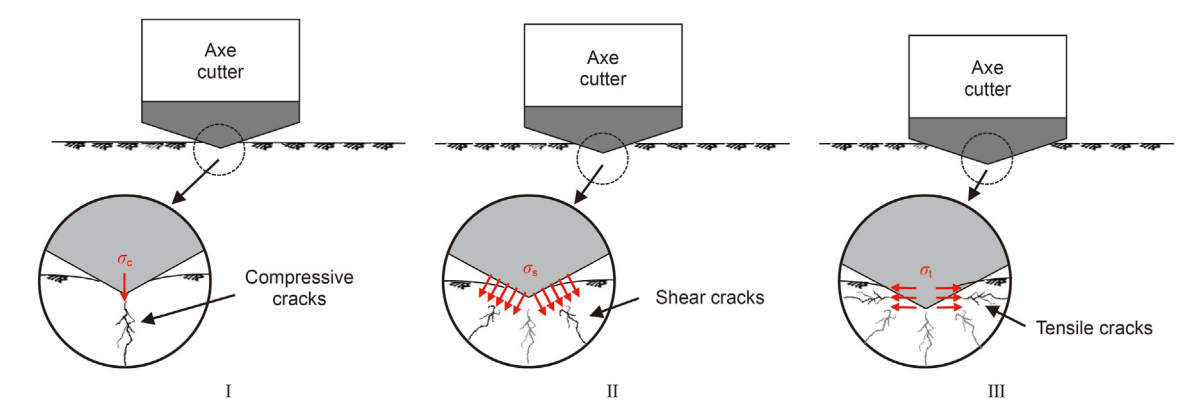


Fig. 25. Rock-breaking mechanism of axe-shaped tooth.

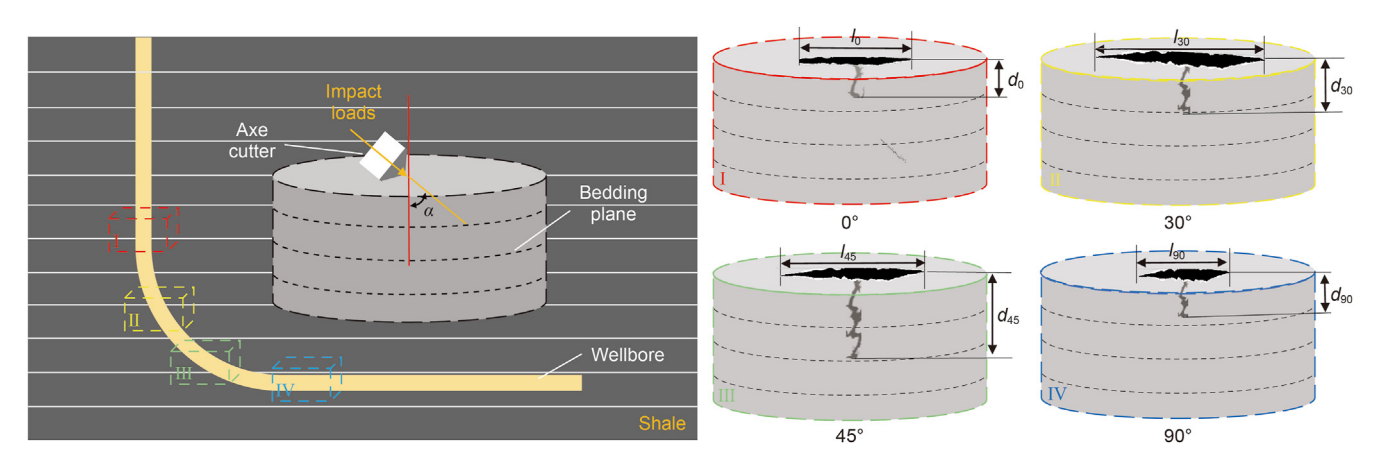


Fig. 26. Schematic of axe-shaped tooth rock-breaking mechanism and shale crack propagation.

during rock breakage. The following significant conclusions are drawn.

- (1) The dynamic properties of the rock are tested under different α . The results show that with the increase of α (0°–90°), the compressive strength first decreases and then increases, presenting a "V"-shaped variation pattern. The strength value is the minimum at $\alpha=45^\circ$, whereas it is the maximum at $\alpha=0^\circ$. The tensile strength first decreases and then increases, whose value is the maximum at $\alpha=30^\circ$ and the minimum at $\alpha=90^\circ$. With the elevation of impact velocity, $\alpha=0$ 0° exerts an increasingly weaker influence on the dynamic compressive strength, with an increasingly significant influence on the dynamic tensile strength.
- (2) The variation trend of the tensile-compression ratio of dynamic strengths is analyzed under different α . When the impact velocity is low (7.0 m/s), the tensile-compression ratio increases, then decreases and increases again, reaching the maximum at α of 90°. When the impact velocity is high (\geq 8.0 m/s), the tensile-compression ratios decrease and then increase, all reaching the minimum at 30° and the maximum at 60°.
- (3) The fragment size distribution pattern of shale after impact crushing is analyzed. With the increase in impact velocity, the rock fragmentation will be more obvious, and the number of generated fragments is generally higher. In the tensile test, when $\alpha=30^\circ$ shale crushing produces the most debris and the size distribution of debris at this time is more

- uniform, which can ensure the cleaning efficiency of the drilling fluid.
- (4) A rock-breaking test with an axe-shaped single tooth under impact loads is undertaken at different α , and the rock fragmentation effect is quantified using a 3D scanning technique. With the increase of α , the penetration depth of the tooth first increases and then decreases, reaching the maximum when $\alpha=45^\circ$. The width of the impact pit generated by tooth penetration first increases and then decreases, reaching the maximum when $\alpha=30^\circ$.
- (5) The anisotropic shale fragmentation mechanism by drill cutter tooth during rock breakage in deep shale gas well is revealed. The results show that under the same impact loads, the drill cutter tooth easily produces a wide range of rock damage when the well inclination is 30° and a significant penetration depth at a well inclination of 45°. The rockbreaking efficiency is the lowest in the horizontal well section.

CRediT authorship contribution statement

Yan Xi: Writing — original draft, Funding acquisition, Conceptualization. **Yu Yao:** Writing — original draft. **Hong-Ao Zhao:** Investigation. **Qian Li:** Resources. **Jun Li:** Methodology. **Ying-Chun Chen:** Writing — review & editing.

Declaration of competing interest

The authors declare no conflict of interest.

Acknowledgement

The current research was financially supported by the National Natural Science Foundation of China (52374001; 52104001).

References

- Akbari, B., Miska, S., 2016. The effects of chamfer and back rake angle on PDC cutters friction. J. Petrol. Sci. Eng. 35, 347–353. https://doi.org/10.1016/j.jngse.2016.08.043.
- Alsuwaidi, E.S., Xi, G.F., Zimmerman, R.W., 2021. Mechanical characterization of laffan and nahr umr anisotropic shales. J. Petrol. Sci. Eng. 200, 108195. https://doi.org/10.1016/j.petrol.2020.108195.
- Amar, M.S.S., Seow, B.C., Za'ba, M.A.Z., Razak, M.K.A., Aziz, W.N.W., 2019. Revolutionary PDC cutter design help improve bit performance in Malay Basin. SPE/IATMI Asia Pacific Oil & Gas Conference and Exhibition, Bali, Indonesia. https://doi.org/10.2118/196465-MS.
- Bobko, C., Ulm, F.J., 2008. The nano-mechanical morphology of shale. Mech. Mater. 40 (4–5), 318–337. https://doi.org/10.1016/j.mechmat.2007.09.006.
- Cao, S.R., Ge, Z.L., Zhang, D., Zhou, Z., Lu, Y.Y., Zhao, H.Y., 2022. An experimental study of ultra-high pressure water jet-induced fracture mechanisms and pore size evolution in reservoir rocks. Int. J. Rock Mech. Min. Sci. 150, 104995. https:// doi.org/10.1016/j.ijrmms.2021.104995.
- Chang, X., Zhang, X., Qian, L.Z., Chen, S.H., Yu, J., 2022. Influence of bedding anisotropy on the dynamic fracture behavior of layered phyllite. Eng. Fract. Mech. 260, 108183. https://doi.org/10.1016/j.engfracmech.2021.108183.
- Chen, P.J., Miska, S., Yu, M.J., Ozbayoglu, E., 2021. Modeling of cutting rock: from PDC cutter to PDC bit—modeling of PDC cutter. SPE J. 26, 3465–3487. https://doi.org/10.2118/205342-PA.
- Cui, J.F., Si, G.Y., 2021. Equivalent anisotropic permeability of shale rocks: effect of micro-fractures. J. Petrol. Sci. Eng. 207, 109085. https://doi.org/10.1016/ j.petrol.2021.109085.
- Deshpande, V.M., Chakraborty, T., 2023. Experimental and numerical study on the dynamic behavior of a transversely isotropic rock. Eng. Geol. 314, 107016. https://doi.org/10.1016/j.enggeo.2023.107016.
- Dong, Z.X., Zhang, H., Li, J., Zhang, K.S., Ou, Y.Y., Lu, Z.Y., Shi, J.G., 2022. A method for evaluating the rock breaking efficiency of cutters and optimizing the PDC cutter profile—a study of igneous rock formations in Shunbei oilfield. Energies 15 (18), 6686. https://doi.org/10.3390/en15186686.
- Fan, X.R., Luo, N., Liang, H.L., Sun, X., Zhai, C., Xie, L.X., 2021. Dynamic breakage characteristics of shale with different bedding angles under the different ambient temperatures. Rock Mech. Rock Eng. 54, 3245—3261. https://doi.org/ 10.1007/s00603-021-02463-6.
- Feng, X.H., Gong, B., Liang, Z.Z., Wang, S.Y., Tang, C.A., Li, H., Ma, T.H., 2023. Study of the dynamic failure characteristics of anisotropic shales under impact Brazilian splitting. Rock Mech. Rock Eng. 57, 2213—2230. https://doi.org/10.1007/s00603-023-03673-w.
- Fjær, E., Nes, O.M., 2014. The impact of heterogeneity on the anisotropic strength of an outcrop shale. Rock Mech. Rock Eng. 47, 1603—1611. https://doi.org/10.1007/ s00603-014-0598-5.
- Gale, J.F.W., Laubach, S.E., Olson, J.E., Eichhuble, P., Fall, A., 2014. Natural fractures in shale: a review and new observations. AAPG Bull. 98 (11), 2165–2216. https://doi.org/10.1306/08121413151.
- Guo, J.C., Zhao, Z.H., He, S.G., Liang, H., Liu, Y.X., 2015. A new method for shale brittleness evaluation. Environ. Earth Sci. 73, 5855–5865. https://doi.org/ 10.1007/s12665-015-4268-z.
- Guo, T.L., Zhang, H.R., 2014. Formation and enrichment mode of Jiaoshiba shale gas field Sichuan basin. Petrol. Explor. Dev. 41 (1), 31–40. https://doi.org/10.1016/ \$1876-3804(14)60003-3
- Guo, Y.D., Li, X.B., Huang, L.Q., 2023. Experimental investigation on the sudden cooling effect of oil-based drilling fluid on the dynamic compressive behavior of deep shale reservoirs. Energy 282, 128680. https://doi.org/10.1016/ i.energy.2023.128680.
- Han, Z.Y., Li, D.Y., Zhou, T., Zhu, Q.Q., Ranjith, P.G., 2020. Experimental study of stress wave propagation and energy characteristics across rock specimens containing cemented mortar joint with various thicknesses. Int. J. Rock Mech. Min. Sci. 131, 104352. https://doi.org/10.1016/j.ijrmms.2020.104352.
- He, R., Ren, L., Zhang, R., Zhu, Z.M., Sun, X., 2022. Anisotropy characterization of the elasticity and energy flow of Longmaxi shale under uniaxial compression. Energy Rep. 8, 1410–1424. https://doi.org/10.1016/j.egyr.2021.12.050.
- He, W., Chen, Z., Shi, H., Li, S., Chen, H., 2021. Numerical analysis on rock-breaking mechanisms of various kinds of ridged PDC cutters. 55th U.S. Rock Mechanics/ Geomechanics Symposium. United states, Houston, Virtual, TX.
- Huang, L.Q., Guo, Y.D., Li, X.B., 2022. Mechanical response to dynamic compressive load applied to shale after thermal treatment. J. Nat. Gas Sci. Eng. 102, 104565. https://doi.org/10.1016/j.jngse.2022.104565.
- Hucka, V., Das, B., 1974. Brittleness determination of rocks by different methods. Int.

J. Rock Mech. Min. Sci. Geomech. Abstracts 11 (10), 389–392. https://doi.org/10.1016/0148-9062(74)91109-7.

- Ju, P., Wang, Z., Zhai, Y.H., Su, D.Y., Zhang, Y.C., Cao, Z.H., 2014. Numerical simulation study on the optimization design of the crown shape of PDC drill bit. J. Pet. Explor. Prod. Technol. 4, 343–350. https://doi.org/10.1007/s13202-013-0091-9.
- Kahraman, S., Bilgin, N., Feridunoglu, C., 2003. Dominant rock properties affecting the penetration rate of percussive drills. Int. J. Rock Mech. Min. Sci. 40 (5), 711–723. https://doi.org/10.1016/S1365-1609(03)00063-7.
- Ke, X.H., Sun, J.S., Yang, X.W., Ma, C., Yu, J.Q., Huang, K.L., 2023. Cutting mechanism of a special 3D concave-shaped PDC cutter applicable to the Weiyuan shale. J. Pet. Explor. Prod. Technol. 13, 1435–1451. https://doi.org/10.1007/s13202-023-01621-6.
- Li, C.X., Ke, X.H., Guo, J.H., Peng, Q., Ma, C., Yu, J.Q., Cheng, C., 2022. Numerical simulation and field verification of the cutting efficiency of 3D shaped PDC cutters. SPE Annual Technical Conference and Exhibition. https://doi.org/ 10.2118/209978-MS.
- Li, X.B., Lok, T.S., Zhao, J., 2005. Dynamic characteristics of granite subjected to intermediate loading rate. Rock Mech. Rock Eng. 38, 21–39. https://doi.org/10.1007/s00603-004-0030-7.
- Liu, H.B., Cui, S., Meng, Y.F., Li, Z., Yu, X.C., Sun, H.R., Zhou, Y.X., Luo, Y., 2021a. Rock mechanics and wellbore stability of deep shale during drilling and completion processes. J. Petrol. Sci. Eng. 205, 108882. https://doi.org/10.1016/j.petrol.2021.108882.
- Liu, R., Jiang, D.C., Zheng, J., Hao, F., Jing, C., Liu, H., Zhang, J.H., Wei, G.D., 2021b. Stress heterogeneity in the Changning shale-gas field, southern Sichuan Basin: implications for a hydraulic fracturing strategy. Mar. Petrol. Geol. 132, 105218. https://doi.org/10.1016/j.marpetgeo.2021.105218.
- https://doi.org/10.1016/j.marpetgeo.2021.105218.

 Negm, S., Aguib, K., Karuppiah, V., ElOufy, M., Remah, M., Zayyan, M., Sheikh, O.E., 2016. The disruptive concept of 3D cutters and hybrid bits in polycrystalline diamond compact drill-Bit design. Abu Dhabi International Petroleum Exhibition & Conference, Abu Dhabi, UAE. https://doi.org/10.2118/183335-MS.

 Peng, Q., Zhou, Y.C., Yu, J.Q., Yang, X.W., Liu, Y., Ma, C., Cheng, C., Ke, X.H., 2022.
- Peng, Q., Zhou, Y.C., Yu, J.Q., Yang, X.W., Liu, Y., Ma, C., Cheng, C., Ke, X.H., 2022.
 Study on rock breaking efficiency of special shaped cutters. IOP Conf. Ser. Earth Environ. Sci. 983, 012089. https://doi.org/10.1088/1755-1315/983/1/012089.
 Qin, X., Zhao, L.X., Cai, Z.J., Wang, Y., Xu, M.H., Zhang, F.S., Han, D.H., Geng, J.H., 2022.
- Qin, X., Zhao, L.X., Cai, Z.J., Wang, Y., Xu, M.H., Zhang, F.S., Han, D.H., Geng, J.H., 2022. Compressional and shear wave velocities relationship in anisotropic organic shales. J. Petrol. Sci. Eng. 219, 111070. https://doi.org/10.1016/ j.petrol.2022.111070.
- Sha, S., Rong, G., Chen, Z.H., Li, B., Zhang, Z.Y., 2020. Experimental evaluation of physical and mechanical properties of geothermal reservoir rock after different cooling treatments. Rock Mech. Rock Eng. 53, 4967–4991. https://doi.org/ 10.1007/s00603-020-02200-5.
- Shao, F.Y., Liu, W., Gao, D.L., Ye, Y.C., 2021. Study on rock-breaking mechanism of axe-shaped PDC cutter. J. Petrol. Sci. Eng. 205, 108922. https://doi.org/10.1016/ j.petrol.2021.108922.
- Shi, X.S., Liu, D.A., Yao, W., Shi, Y.R., Tang, T.W., Wang, B.N., Han, W.G., 2018. Investigation of the anisotropy of black shale in dynamic tensile strength. Arabian J. Geosci. 11, 42. https://doi.org/10.1007/s12517-018-3384-y.
- Turcotte, D.L., 1986. A fractal model for crustal deformation. Tectonophysics 132 (1–3), 261–269. https://doi.org/10.1016/0040-1951(86)90036-3.
- Wang, P., Xu, J.Y., Fang, X.Y., Wang, P.X., 2017. Energy dissipation and damage evolution analyses for the dynamic compression failure process of redsandstone after freezethaw cycles. Eng. Geol. 221, 104–113. https://doi.org/ 10.1016/j.enggeo.2017.02.025.
- Wang, P., Yin, T.B., Li, X.B., Zhang, S.S., 2019. Dynamic properties of thermally treated granite subjected to cyclic impact loading. J. Nat. Gas Sci. Eng. 52, 991–1010. https://doi.org/10.1007/s00603-018-1606-y.
- Wang, X.Y., Zhu, Z.M., Zhou, L., Ma, L.J., Zhou, C.L., Wang, Z.H., 2022. Study on the effects of joints orientation and strength on failure behavior in shale specimen under impact loads. Int. J. Impact Eng. 163, 104162. https://doi.org/10.1016/ j.ijimpeng.2022.104162.
- Wong, L.N.Y., Zou, C.J., Cheng, Y., 2014. Fracturing and failure behavior of Carrara marble in quasistatic and dynamic Brazilian disc tests. Rock Mech. Rock Eng. 47, 1117–1133. https://doi.org/10.1007/s00603-013-0465-9.
- Xi, Y., Wang, W., Fan, L.F., Zha, C.Q., Li, J., Liu, G.H., 2022a. Experimental and numerical investigations on rock-breaking mechanism of rotary percussion drilling with a single PDC cutter. J. Petrol. Sci. Eng. 208 (B), 109227. https://doi.org/10.1016/j.petrol.2021.109227.
- Xi, Y., Wang, W., Zha, C.Q., Li, J., Liu, G.H., 2022b. Numerical investigations on rock breaking mechanism and parameter influence of torsional percussive drilling with a single PDC cutter. J. Petrol. Sci. Eng. 210, 110077. https://doi.org/10.1016/ j.petrol.2021.110077.
- Xi, Y., Wang, H.Y., Li, J., Jiang, H.L., Fan, L.F., 2023. Transient process of mechanical response and energy conversion of rocks with different lithologies under impact loading. Geoenergy Science and Engineering 228, 211978. https:// doi.org/10.1016/j.geoen.2023.211978.
- Yang, G.L., Bi, J.J., Li, X.G., Liu, J., Feng, Y.J., 2020. SHPB testing and analysis of bedded shale under active confining pressure. J. Eng. 5034902. https://doi.org/10.1155/ 2020/5034902
- Yang, S.Q., Yin, P.F., Li, B., Yang, D.S., 2020. Behavior of transversely isotropic shale observed in triaxial tests and Brazilian disc tests. Int. J. Rock Mech. Min. Sci. 133, 104435. https://doi.org/10.1016/j.ijrmms.2020.104435.
- Yin, Z.Q., Li, X.B., Jin, J.F., He, X.Q., Du, K., 2012. Failure characteristics of high stress rock induced by impact disturbance under confining pressure unloading. Trans. Nonferrous Metals Soc. China 22 (1), 175–184. https://doi.org/10.1016/S1003-

6326(11)61158-8.

- Zhang, J., Deng, H.W., Taheri, A., Ke, B., Liu, C.J., Yang, X.R., 2018. Degradation of physical and mechanical properties of sandstone subjected to freeze-thaw cy-cles and chemical erosion. Cold Reg. Sci. Technol. 155, 37–46. https://doi.org/ 10.1016/j.coldregions.2018.07.007.
- Zhang, Z.Y., Qian, Q.Y., Wang, H., Huang, Y.H., Wang, J.G., Liu, H.S., 2021. Study on the dynamic mechanical properties of metamorphic limestone under impact loading. Lithosphere 8403502. https://doi.org/10.2113/2021/8403502.
 Zhao, Z.Y., Xue, J.C., Jin, J.F., Tan, L., Xia, W.B., Cai, R.Y., 2023. Experimental research on the dynamic constringent characteristics and fractal properties of sandstone
- under impact loading. Case Stud. Constr. Mater. 18, e02174. https://doi.org/ 10.1016/j.cscm.2023.e02174.
- Zhou, Y.X., Xia, K., Li, X.B., Li, H.B., Ma, G.W., Zhao, J., Zhou, Z.L., Dai, F., 2012. Suggested methods for determining the dynamic strength parameters and mode-I fracture toughness of rock materials. Int. J. Rock Mech. Min. Sci. 49, 105–112.
- https://doi.org/10.1016/j.ijrmms.2011.10.004.

 Zhu, X.H., Luo, Y.X., Liu, W.J., Yang, F.L., Li, Z.L., Lu, D.Y., 2022. Rock cutting mechanism of special-shaped PDC cutter in heterogeneous granite formation. J. Petrol. Sci. Eng. 210, 110020. https://doi.org/10.1016/j.petrol.2021.110020.